PLASMA ACTUATORS FOR SEPARATION CONTROL ON STATIONARY AND OSCILLATING AIRFOILS

A Dissertation

Submitted to the Graduate School
of the University of Notre Dame
in Partial Fulfillment of the Requirements
for the Degree of

Philosophy of Science in Aerospace and Mechanical Engineering

by

Martiqua L. Post, M.S.M.E.

Thomas C. Corke, Director

Department of Aerospace and Mechanical Engineering
Notre Dame, Indiana
May 2004

PLASMA ACTUATORS FOR SEPARATION CONTROL ON STATIONARY AND OSCILLATING AIRFOILS

ABSTRACT

by

Martiqua L. Post

This thesis deals with the development of phased plasma actuators for use in separation control on helicoptor rotor blades. Plasma, or ionized air, is generated by high voltage a.c. signals which are sent to an array of surface electrodes. The plasma induces a body force, which in one-dimension is recognizable as a pressure gradient. In this work, the electrode configuration was optimized and tested to determine the effects of the plasma actuators on the surrounding flow.

To optimize the plasma actuator, numerical simulations modeled the relative effect of the net body force. Flow visualization images indicated that very different results were produced by varying the orientation, the voltage input, frequency difference, or phase shift of the electrodes. For example, the upstream oriented electrode array resulted in the formation of recirculation regions above each electrode, while the downstream oriented array produced a wall-jet, which energized and accelerated the flow at the wall. Configurations which should be effective for separation are presented.

A plasma actuator at the leading edge of a NACA 0015 airfoil was used to control flow separation for high angle of attack stationary and periodic oscillating conditions. The effectiveness of the actuator was documented through pressure measurements on the surface of the airfoil, mean velocity profiles in the airfoil wake, and flow visualization records. For the oscillating airfoil, the measurements were phase conditioned to the oscillation motion. For the stationary airfoil, the actuator prevented flow separation for angles of attack up to 22°, which was 8° past the static stall angle. This resulted in as much as a 300% improvement in the lift-to-drag ratio. The oscillating airfoil was driven in a periodic cycle corresponding to $\alpha = 15^\circ + 10^\circ \sin \omega t$. The results for a reduced frequency of $k = \omega c / 2\nu = 0.08$ are presented here. Three cases with the plasma actuator were investigated: steady actuation, unsteady plasma actuation, and so-called "smart" actuation in which the actuator is activated in selected portions of the oscillatory cycle. All of the cases exhibited a higher cycle-integrated lift and an improvement in the lift cycle hysteresis.

For my Mother,

Words cannot express everything you
have done for me … thank you
for all your love and support.

CONTENTS

LIST OF TABLES

LIST OF FIGURES

LIST OF SYMBOLS

English symbols

$a.c.$	alternating current
B_E	body force induced by electric field
c	chord
c_a	axial force coefficient
c_n	normal force coefficient
C_d	coefficient of drag
C_l	coefficient of lift
C_p	coefficient of pressure
C_μ	momentum coefficient
d	distance between upper and lower electrodes
$d.c.$	direct current
e	electronic charge
E	electric field strength
f_o	travelling wave frequency [Hz]
f_1	frequency to lower electrodes
f_2	frequency to upper electrodes
h	jet slot height
H	total test section height
I	current
k	reduced frequency
k	Boltmann's constant

m	mass
n_e	electron density
n_i	ion density
n_o	background plasma density
N	number of electrodes
P	pressure
Re	Reynolds number
RF	ratio-frequency
RBS	Retreating Blade Stall
s	spacing between electrodes
t	time [sec]
T	temperature
U_{act}	velocity produced by flow control actuator
$U_{induced}$	velocity generated by steady plasma
U_{phase}	phase velocity
U_∞	freestream velocity
V	voltage
V_{p-p}	peak-to-peak voltage
V_{rms}	root-mean-square voltage
x	distance in the x-direction
y	distance in the y-direction
z	distance in the z-direction

Greek symbols

α	angle of attack
α_0	mean angle of attack
α_1	alternating angle of attack
Δ	change in
Ω	ohms
ω	physical frequency
ϵ_o	permittivity of free space
ϕ	local electric potential
ρ	density
λ_D	Debye length
τ	period

CHAPTER 1

INTRODUCTION

1.1 Motivation

The maximum lift and stall characteristics of a wing affect many performance aspects of aircraft including take-off and landing distance, maximum and sustained turn rates, climb and glide rates, and flight ceiling [10]. In a 2-D wing, the maximum achievable lift is ultimately limited by the ability of the flow to follow the curvature of the airfoil. When it cannot, the flow separates. In most cases, this first occurs at the leading edge.

One solution to prevent leading-edge separation is to increase the leading edge radius. This is the principle effect of a leading edge flap. An example is a Krueger flap, which consists of a hinged surface on the lower side of the wing leading edge that can extend out and ahead of the wing leading edge. A slotted leading-edge flap (slat) is the leading-edge equivalent of the trailing-edge slotted flap. It works by allowing air from the high-pressure lower surface to flow to the upper surface to add momentum to the boundary layer and prevent flow separation.

Although these leading edge devices are effective, they have some drawbacks. In particular they are complicated, add weight to the wing, take volume from inside the wing when not in use, and can be major sources of airframe noise and vibration. Therefore if they can be replaced by other flow control devices, there could be a number of benefits.

Helicopter rotors are wing sections which have the added complication that they need to cycle in angle of attack to control the lift vector for translational flight. During portions of the retreating phase of the rotor, the rotor flow separates (stalls) due to a combination of high angles of attack and a lower effective velocity. This ultimately limits the payload capability and flight performance of the helicopter.

The passive devices typically effective on fixed wings are impractical on helicopter rotors because they would have to be deployed in a rapid, time-dependent manner in the rotor cycle. In addition, the helicopter rotor is a finely engineered composite structure that has to be able to withstand high centrifugal loading. Any moving or deployable elements on the rotor would be subjected to the same high loading levels. Even the addition of slots or internal cavities in the rotor could present a significant compromise in the structural integrity of the rotor.

1.2 Background

This section provides background information on separation control techniques, airfoil aerodynamics, and rotor aerodynamics.

1.2.1 Separation Control Techniques

Attempted solutions to flow separation include prevention, reduction, or elimination. Several flow control techniques that have been investigated for leading-edge separation include (but are not limited to) boundary layer mixing [5, 80], removal of low-momentum from near-wall flow [20, 74], and momentum addition to near-wall flow [51, 76].

Separation of flow from a surface is governed by the adverse pressure gradient and viscosity. To remain attached to the surface, the flow must have sufficient energy to overcome the adverse pressure gradient, the viscous dissipation along the flow path, and the energy loss due to the change in momentum. When it does not have enough energy, the *separates* from the surface. Techniques for flow control are designed to augment the energy level by a device or actuator at the appropriate position along the flow path. This section introduces the following control methods:

1. Boundary Layer Mixing
2. Removal of Low-Momentum from Near-Wall Flow
3. Momentum Addition to Near-Wall Flow

Boundary Layer Mixing

The purpose of boundary layer mixing is used to transport momentum from the freestream to the boundary layer. One technique to induce boundary layer mixing is vortex generators. These devices are small plates or airfoils mounted normal the surface and set at an angle of incidence with respect to the local flow direction. The result is an array of near wall trailing, streamwise vortices embedded within the boundary layer. These streamwise vortices bring high momentum fluid into the boundary layer to prevent flow separation.

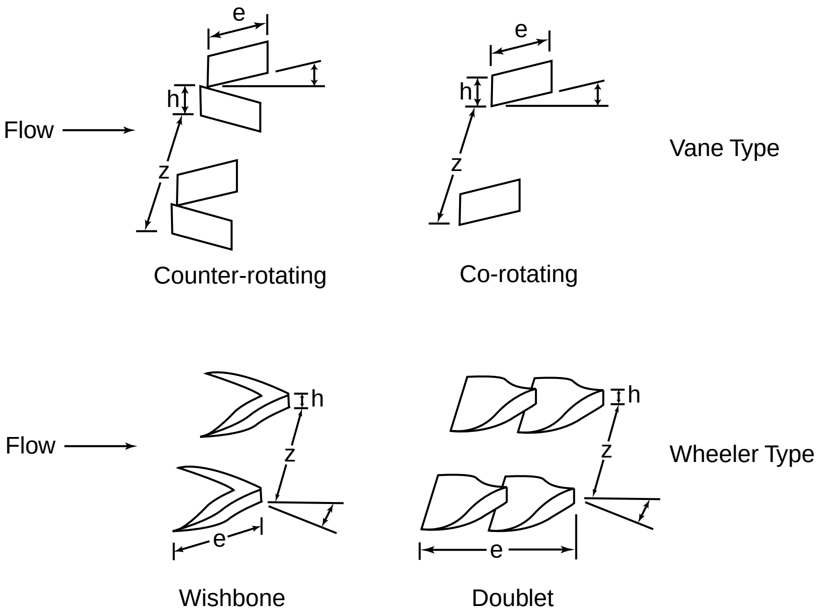

Figure 1.1. Schematic of types of passive vortex generators.

Passive vortex generators have been in use since the 1940's by Taylor [85]. The VG height, h, is typically on the order of the boundary layer thickness, δ. The spacial relationship between each individual generator is also important. Large counter-rotating vortices force regions of vorticity to rise above the surface reducing their effect, while too closely spaced co-rotating vortices combine to form one large vortex, also reducing the overall effect. A schematic of the various type of vortex generators are shown in Figure 1.1.

Schubauer and Spangenberg investigated effect of fixed, mixing devices on the boundary layer on a flat plate [80]. They found that mixing on a coarse scale by relatively large, widely-spaced devices was far more effective than fine-scale mixing and that multiple rows were less effective that a single row of devices properly-spaced and stationed. It was concluded that forced mixing (with VG-like structures) had "basically" the same effect on the boundary layer as a general reduction in pressure gradient.

Low-profile vortex generators are defined as those with a device height, h, between 10% and 50% of the boundary layer thickness, δ. These devices are most useful where flow separation locations are reasonably fixed. Placed reasonably close upstream of the separation, they can produce streamwise vortices just strong enough to overcome the separation without persisting within the boundary layer once the flow control objective is achieved. The most effective range of low-profile VGs has been determined to be about $5h - 30h$ upstream of the baseline separation, although the device-induced streamwise vortices could last up to $100h$ [47].

Due to the simplicity of the vortex generators, they have been frequently applied, but the effectiveness of this method can be limited because of their parasitic drag.

Removal of Low-Momentum from Near-Wall Flow

Boundary layer suction is used to prevent laminar or turbulent separation by removing the low momentum flow from the boundary layer. The principle is to remove the decelerated fluid before it can separate from the surface. Removing the fluid particles in the near-wall region increases the velocity gradient at the wall, and the curvature of the velocity profile near the surface becomes more negative. This eliminates the viscosity effect and prevents boundary layer growth, and a new boundary layer is formed downstream of the suction area. Therefore, by using suction upstream of the separation location, flow separation may be prevented.

There are two techniques for suction; discrete (slot) suction and continuous suction. Discrete suction abruptly increases the pressure at the location of the slot. Continuous suction is done though a porous surface, which allows for a gradual decrease in pressure along the surface.

One major concern with the suction technique being employed on an operational wing, is physical surface contamination. Contamination, caused by ice, rain, dust, pollen, and insects, may block suction slots or holes which results in a consequent loss of suction. Another concern is that the development of a boundary layer suction system is quite complicated. It involves considerations on optimum slot placement and amount of suction, structural modifications to the wind tunnel or experimental model to include suction chambers, and a power system [25]. These issues have discouraged its use on the wings of aircraft.

Momentum Addition to Near-Wall Flow

High momentum flow supplied to the boundary layer can control flow separation. The near-wall velocity profile can be modified by actively discharging fluid from the body (by blowing) or passively by deriving the energy directly from the freestream (from a leading edge slat). These two methods for adding momentum to the near-wall flow are illustrated schematically in Figure 1.2.

Leading-edge Slat

A slotted leading-edge flap (slat) works by allowing air from the high-pressure lower surface to flow to the upper surface to add momentum to the boundary layer and prevent flow separation. The momentum comes directly from the freestream.

A Krueger flap, which consists of a hinged surface on the lower side of the wing

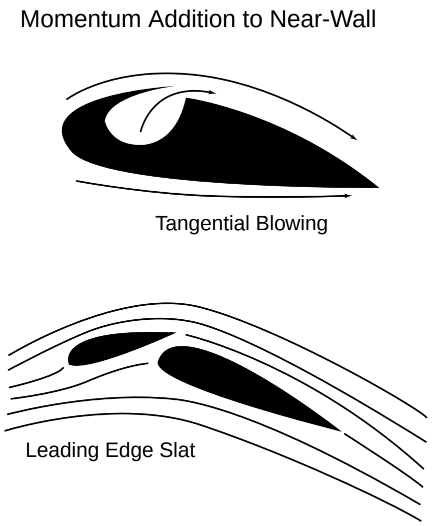

Figure 1.2. Methods to add high momentum fluid to the near-wall flow.

leading edge that can extend out and ahead of the wing leading edge, effectively increases the leading edge radius while adding momentum to the boundary layer. This technique does not require any direct energy cost; however, the blowing intensity is limited by the pressure differentials on the body.

Unfortunately, the leading edge slat, under certain flight conditions, can be a major source of airframe noise. Broadband noise has been attributed to the interaction of the reattached shear layer in the slat cusp with the slat trailing edge. Tonal noise sources associated with the leading edge slat are due to trailing edge vortex shedding [59]. Much effort is underway to determine the physics behind the sources of noise and to apply this knowledge to developing noise reduction technologies [41, 56, 59].

Tangential Steady Blowing

The blowing of a thin jet upstream or in the region of separation increases the energy in the boundary layer and can be an effective method to control flow separation. The lost energy in the boundary layer is replaced with the momentum of fluid blowing tangentially from the wall. The jet flow only affects the velocity profile in the boundary layer. Since blowing increases the velocity in the near-wall region, it is apparent that separation can be prevented by blowing.

In general, blowing techniques are very effective in controlling separation; however, to obtain this degree of control requires the complexity and cost of internal piping from pressure source. The energy required to prevent the flow separation must be less than the energy gained by the effective separation control. Compressed air from a jet engine compressor may be used for blowing, and the high pressure air bleed can be bled to a choked blowing slot [9]. High pressure air can be used enabling relatively small interior piping as opposed to suction control, while generally more efficient than blowing at both low and high speeds, usually requires more piping [26].

Dynamic Forcing

Both tangential blowing to supply high momentum and large coherent structure generation to transport momentum (vortex generators), when used separately, have been investigated and proven to be successful methods in controlling the boundary layer [9, 80]. Therefore, a combination of the two may be very effective in boundary layer control. Tangential blowing coupled with the introduction of a periodic disturbance could accelerate and regulate the generation of large coherent structures. This intermittently brings high momentum fluid to the surface, enabling the flow to withstand the adverse pressure gradient without separating.

Figure 1.3 illustrates the concept of dynamic forcing which involves low-level

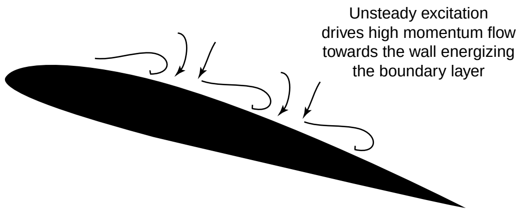

Figure 1.3. Unsteady periodic excitation concept for flow control.

periodic forcing to modulate the formation of large scale, phase-locked coherent vortex structures over the downstream surface. This method acts upon the natural instability of the separated shear layer to perturbations. A perturbation located on the surface of an airfoil can be amplified and propagated by the flow. This effect is further enhanced by a small amount of steady blowing that is also added to the flow [76].

Periodic excitation by oscillatory blowing has been documented extensively by Seifert et al. [76, 77, 78, 79] and in the review by Greenblatt and Wygnanski [32]. The effectiveness of this method is largely determined by the receptivity of the flow to the imposed disturbances; therefore, the disturbances must be introduced at the proper location and be of the correct scale. The amplitude of the imposed oscillations should peak near the separation point. This also coincides with the most efficient position of the actuator location.

The scale of the disturbances found to be most effective was that in which the chord of the airfoil was related to the average frequency of the imposed disturbance. This relationship is defined as the dimensionless frequency parameter, $F+$, and is given by

$$F+ = \frac{fx}{U_\infty}, \tag{1.1}$$

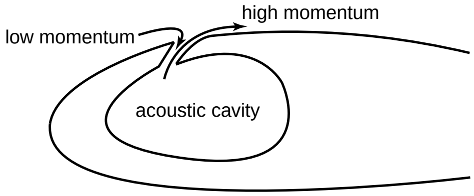

Figure 1.4. Concept of the directed synthetic jet (DSJ).

where f is the frequency of the imposed disturbance, x is the streamwise length from the point of the excitation location to the flap trailing edge, and U_∞ is the freestream velocity. At or near an optimal frequency of $F+ = 1$, nominally 2-3 coherent structures are present over the surface [51].

Directed synthetic jets (DSJ) use the same concept of dynamic forcing to control separation [30, 51, 52, 81]. The synthetic jet consists of an orifice, or neck, driven by an acoustic source in a cavity. During the instroke of the neck velocity, low momentum flow from the incoming boundary layer is sucked into the cavity. During the outstroke, the fluid particles are accelerated and injected with a higher momentum back into the flow. Figure 1.4 illustrates the concept of the zero net flux, direct synthetic jet.

1.2.2 Airfoil Aerodynamics

Airfoils are two-dimensional wing sections or "lifting-surfaces". The resultant forces and moments acting on an airfoil are the net result of the action of the distributed pressure and viscous shear stress. Figure 1.5 shows the pressure and shear forces acting on an element of the airfoil surface. These forces and moments are obtained by integrating the local values of pressure and shear stress acting normal and parallel to the surface around the airfoil. These forces can be resolved into a chord-axis system with normal and axial forces or a wind-axis system with lift and drag forces. Figure 1.6 is a schematic of the decomposition of the resultant forces on and airfoil.

For the normal and lift force, the pressure force dominates and surface shear contributions are negligible. For the axial and drag force, the shear stress contribution has a measurable effect and must be taken into account. The surface pressure data is typically presented in terms of the pressure coefficient, C_p. In compressible flow, the definition of the coefficient of pressure comes from Bernoulli's equation,

$$p_\infty + \frac{1}{2}\rho_\infty U_\infty^2 = p + \frac{1}{2}\rho_\infty U^2 \tag{1.2}$$

where p and U are the local pressure and velocity and p_∞ and U_∞ refers to the freestream pressure and velocity at infinity. The pressure coefficient is defined as the difference between local and freestream pressure divided by the dynamic pressure.

$$C_p = \frac{p - p_\infty}{\frac{1}{2}\rho_\infty U_\infty^2}. \tag{1.3}$$

For an airfoil, the normal, axial, and moment force coefficients can be expressed in terms of the coefficient of pressure, as

$$C_n = \int_0^1 (C_p^L - C_p^U) d\left(\frac{x}{c}\right), \tag{1.4}$$

$$C_a = \int_0^1 \left(C_p^U\left(\frac{dy_U}{c}\right) - C_p^L\left(\frac{dy_L}{c}\right)\right) d\left(\frac{x}{c}\right), \tag{1.5}$$

and

$$C_{m_{LE}} = -\frac{1}{c^2}\int_0^1 (C_p^L - C_p^U)\frac{x}{c} d\left(\frac{x}{c}\right). \tag{1.6}$$

The normal force coefficient can be used interchangeably with the lift coefficient at low angles of attack. However, more accurately the lift coefficient can be calculated

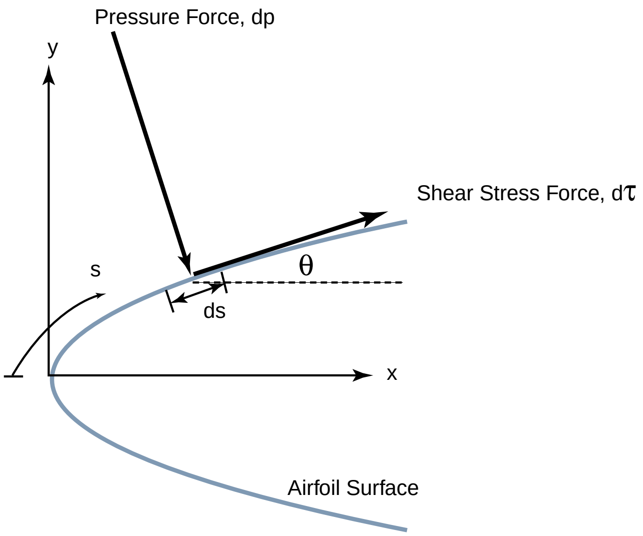

Figure 1.5. Pressure and shear forces acting on an element of the airfoil surface.

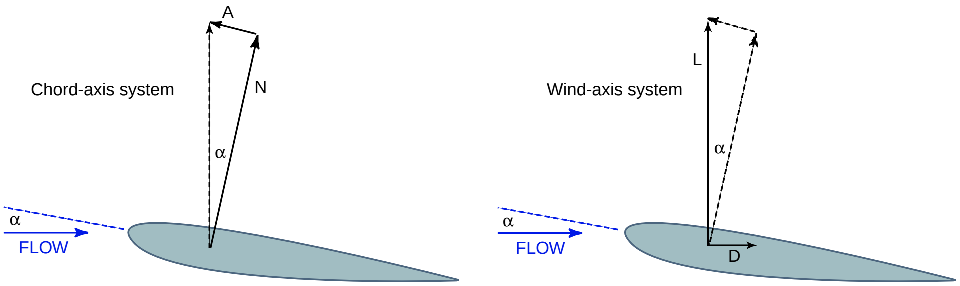

Figure 1.6. Schematic of the decomposition of resultant forces on and airfoil, adapted from Leishman [45].

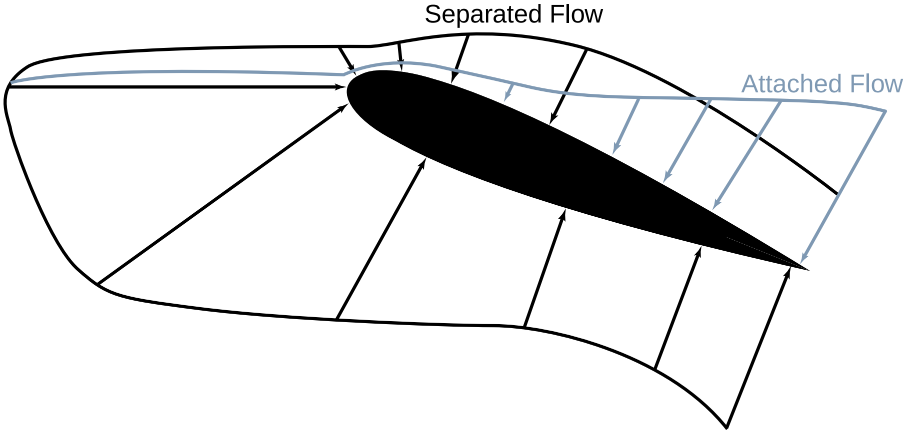

Figure 1.7. Qualitative comparison of the pressure distribution over an airfoil, adapted from Anderson [2].

from both the normal and axial forces and the angle of attack as

$$C_l = C_n \cos\alpha - C_a \sin\alpha. \tag{1.7}$$

Figure 1.7 illustrates a qualitative comparison of the pressure distribution over an airfoil at a high angle of attack. The pressure always acts normal to the surface of the airfoil; therefore, the arrows are all perpendicular to the surface. The aerodynamic lift on the airfoil is derived from the net component of the pressure distribution in the vertical direction. Lift is obtained when the pressure on the bottom surface is large and the pressure on the top surface is small. When the flow separates, the pressure distribution on the bottom surface does not change, but the pressure distribution on the top surface indicates a higher pressure, as shown in Figure 1.7.

Abbott and von Doenoff have documented a summary of airfoil section measurements [1]. These provide a consistent basis from which to review the stall characteristics of airfoils in general.

1.2.3 Helicopter Aerodynamics

Current rotorcraft designs require significant improvements to accommodate the demand for high performance helicopters. In helicopters and other rotorcraft, retreating blade stall (RBS) is the problem which establishes the limits on rotor load and flight speed and subsequently maneuverability and undesirable acoustics.

The retreating blade is the rotor blade that is moving opposite the direction of flight, and the advancing blade moves with the direction of flight. Figure 1.8 shows that the airspeed of the retreating blade slows down as forward speed increases, while the airspeed of the advancing blade increases. Therefore, as the airspeed of the retreating blade decreases with forward air speed, the blade angle of attack must be increased to equalize lift throughout the blade areas. As the angle of attack of the retreating blade continues to increase, the blade will stall at some high, forward speed.

Figure 1.9 shows the hovering lift pattern for a helicopter. A small, no-lift area surrounds the blade root area. As the forward speed of the rotorcraft increases to a normal cruise speed, the no-lift area moves from the center toward the retreating side, as illustrated in Figure 1.10. More lift at the outer retreating blade portions is required to compensate for the loss of lift of the inboard retreating sections.

In the area of reversed flow, the rotational velocity of this blade section is slower than the aircraft airspeed so that the air flows from the trailing edge to the leading edge of the airfoil. In the areas of negative stall and negative lift, the rotational velocity of this blade section is faster that the aircraft airspeed so the air flows from

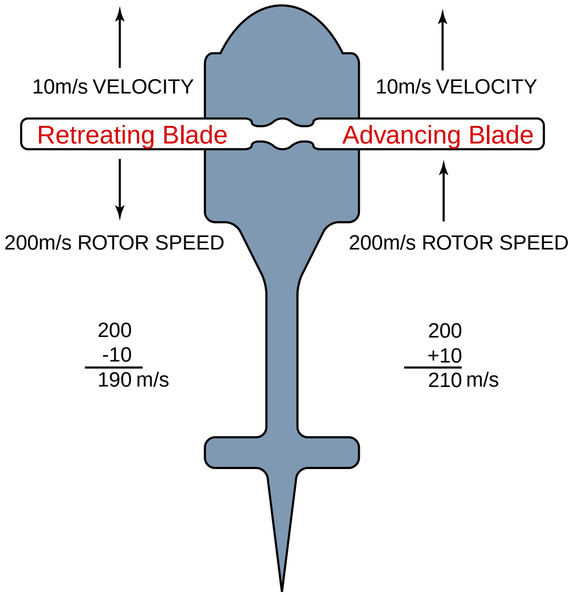

Figure 1.8. The retreating blade moves slower than the advancing blade.

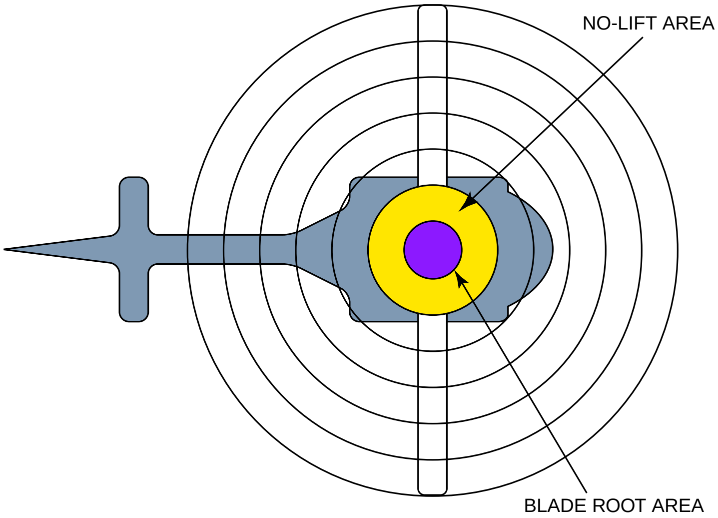

Figure 1.9. Hovering lift pattern of a helicopter.

the leading edge to the trailing edge of the airfoil; however, other issues inhibit a positive angle of attack. The remaining area of the retreating blade must produce as much lift as the entire advancing blade. Therefore the retreating blade operates at much higher angles of attack than the advancing blade.

The lift pattern at critical airspeeds is shown in Figure 1.11. The no-lift area stretches further from the blade root to the retreating blade, and also extends to cover large portions of the blade tip region. When the small area near the tip of the blade stalls, vibration and noise begins. At greater angles of attack, the stall area spreads inward, causing the helicopter to pitch up and roll left.

One important non-dimensional parameter used in rotor aerodynamics is the reduced frequency. This parameter is used to characterize the degree of unsteadiness in the problem. The reduced frequency, k, is normally defined as

$$k = \frac{\omega c}{2U_\infty}, \tag{1.8}$$

where ω is the physical oscillating frequency, c is the airfoil chord, and U_∞ is the freesteam velocity. For $k = 0$ the flow is steady. For $0 \leq k \leq 0.05$ the flow is quasi-steady, meaning the unsteady effects are small and for some problems can be negligible. Flow with $k > 0.05$ are considered unsteady. For a typical helicopter rotor with blade aspect ration $R/c \approx 10$, the reduced frequency is 0.07, which is in the unsteady range.

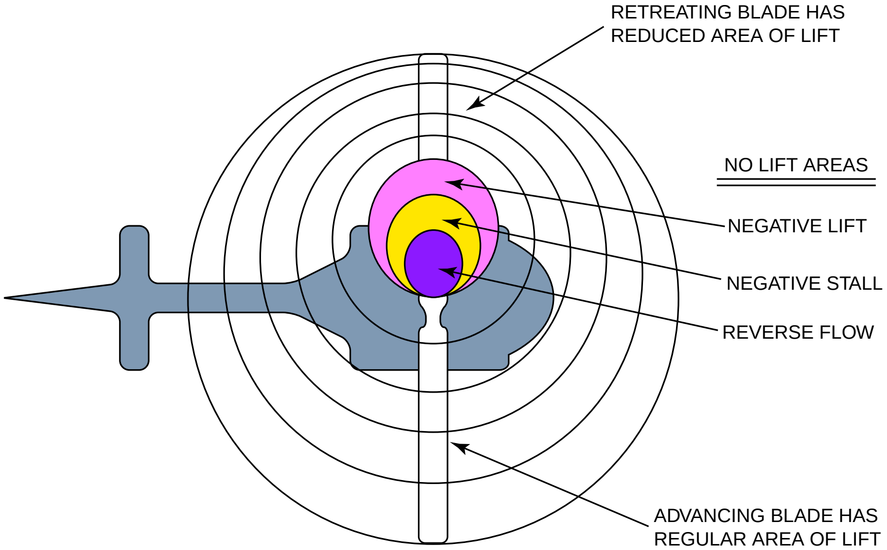

Figure 1.10. Normal cruise lift pattern of a helicopter.

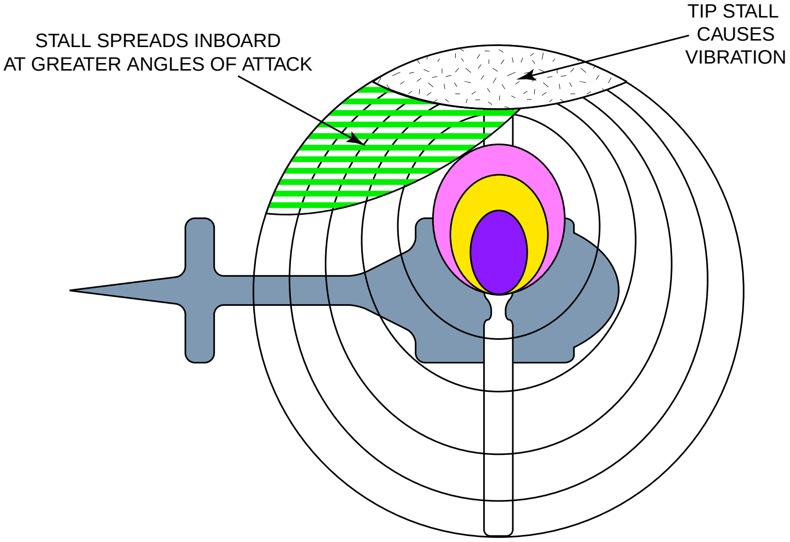

Figure 1.11. Lift pattern of a helicopter at critical speeds.

1.2.3.1 Dynamic Stall

Dynamic stall will occur on any airfoil when it is subjected to time-dependent unsteady motion that takes the effective angle of attack above its normal static stall angle [45]. The dynamic stall physics of flow separation are fundamentally different than static stall. Dynamic stall is characterized by the shedding of a concentrated vortical disturbance from the leading-edge of the airfoil. While the vortical disturbance remains over the suction surface of the airfoil, it acts to enhance the lift being produced. Once the disturbance is convected off the airfoil, a drastic drop in lift is the result.

Figure 1.12 is a schematic detailing several stages of the dynamic stall process. During stage 1 the airfoil exceeds the static stall angle and flow reversals take place in the boundary layer. Stage 2 involves flow separation and the formation of a vortex disturbance at the leading-edge of the airfoil. This vortex provides additional lift on the airfoil as long as it stays over the airfoil suction surface, in stage 3. During stage 4 the flow progresses to a state of full separation, which is accompanied by a sudden loss of lift. Flow reattachment occurs once the angle of attack of the airfoil is low enough in stage 5. Full flow reattachment may not be obtained until well below its normal static stall angle because there is a general lag in reorganization of the flow from the fully separated state.

The knowledge of the effects of unsteady motion on unsteady airfoils and dynamic flow separation are mainly based on research on oscillating airfoils in wind tunnel experiments.

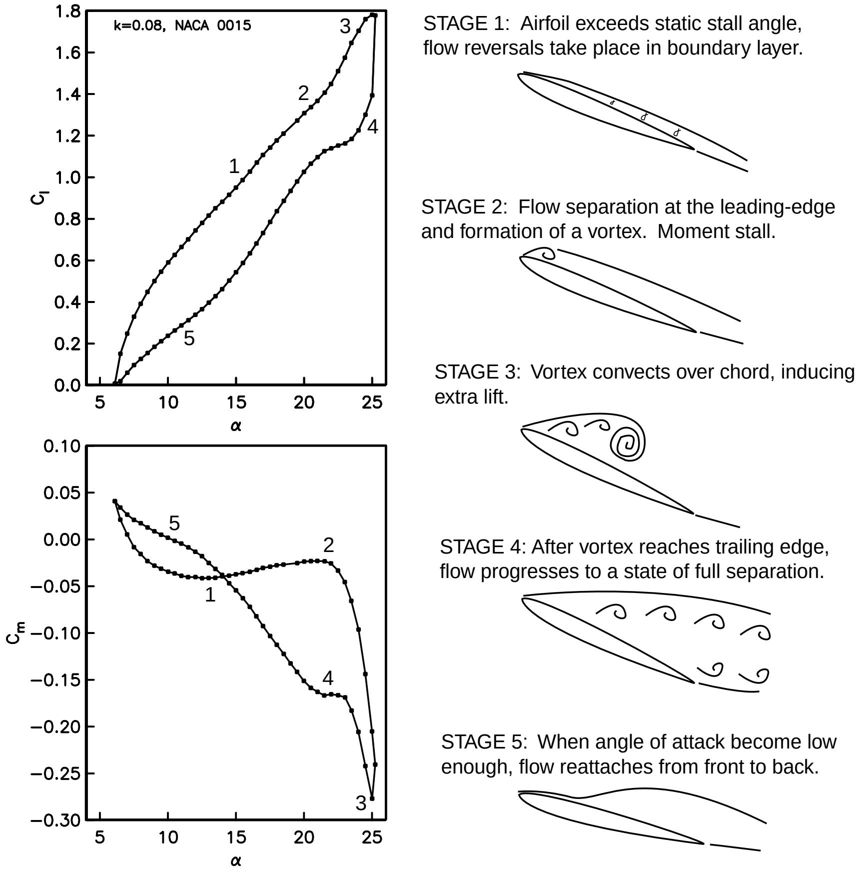

STAGE 1: Airfoil exceeds static stall angle, flow reversals take place in boundary layer.

STAGE 2: Flow separation at the leading-edge and formation of a vortex. Moment stall.

STAGE 3: Vortex convects over chord, inducing extra lift.

STAGE 4: After vortex reaches trailing edge, flow progresses to a state of full separation.

STAGE 5: When angle of attack become low enough, flow reattaches from front to back.

Figure 1.12. Schematic of dynamic stall process. Adapted from Leishmann [45].

1.3 Research Overview and Objectives

The primary objective of this research was to experimentally investigate and characterize the effects of a single-dielectric barrier discharge plasma actuator. At the onset of this research, little was known about the physics or effects of the plasma actuator. Therefore the goals of this research were two-fold: (1) characterize the effects of the plasma actuators at different conditions and determine the important parameters associated with actuator response and (2) document the effectiveness of the plasma actuator in controlling leading-edge separation.

The first goal was to characterize the effects of the plasma actuators at different conditions and determine the important parameters associated with actuator response. This was achieved through a systematic set of experiments conducted in a box with no mean flow. The physical actuator configuration, input versus output relations, and different types of operation (steady and unsteady) were investigated. These results are important in further optimization of the actuator and in sizing the actuators for higher-speed full-scale designs.

The second goal was to document leading-edge separation control using actuators on stationary and oscillating airfoils at high angles of attack. The oscillating airfoil work focuses on the application of controlling retreating blade stall on helicopter rotors. The effectiveness of the actuator for separation control was based on flow visualization, pressure coefficient measurements on the surface of the airfoil from which lift could be derived, and mean velocity measurements in the wake of the airfoil from drag could be derived. Parameters of interest included the actuators configuration, optimum actuator placement, and minimum power requirements.

From these issues stemmed the development and investigation of a plasma flow control device. The approach used here to control separation on both fixed wings and helicopter rotors is the use of plasma actuators [14, 65]. The plasma actuator consists of two copper electrodes separated by a dielectric insulator. The electrodes are supplied with a high (order 3-12 kV_{p-p}) a.c. voltage. When the voltage is sufficiently high, the surrounding air ionizes and plasma forms in the regions of high electrical field potential. These regions are generally located at the edges of the electrode(s) exposed to the air. The ionized air, in the presence of an electric field gradient, results in a body force on the flow [18]. The body force is a vector that can be tailored for a given application through the orientation and design of the electrode geometry

The idea behind developing a new flow control device is first to understand the important flow parameters behind the performance of the actuator. With that knowledge, applications of the actuator can be investigated. This was the process of the the current investigation, an effort to experimentally determine important actuator parameters and document the separation control effectiveness of the actuator on stationary and oscillating airfoils.

Since the onset of this work, the plasma actuators have been successfully used in numerous flow control applications. These include lift augmentation on a wing section [13], low-pressure turbine blade separation control [34], unsteady vortex generation [60, 61], and airfoil leading-edge separation control [66, 67, 68].

This dissertation begins with the background for this research. Chapter 2 presents the theory and optimization of the plasma actuator It described the physical configuration, electronics used to generate the plasma, advantages, and operation of the actuator, as well as the fluid response to the actuator. Chapter 3 documents the experimental facilities and instrumentation used for this study. Chapter 4 embodies the results of the separation control using the plasma actuator on a stationary airfoil. Chapter 5 presents the results of the plasma actuator for separation control on the oscillating airfoil. Conclusions from the research are in Chapter 6.

CHAPTER 2

THE PLASMA ACTUATOR: THEORY & OPTIMIZATION

2.1 Theory

2.1.1 Physical Configuration

The plasma actuator consists of two copper electrodes separated by a dielectric insulator, as illustrated in Figure 2.1. The upper electrode is exposed to the surrounding air and the lower electrode is completely insulated. The geometry of the electrodes is asymmetric, with a small amount (order of a mm) of overlap.

The electrodes were made from 0.025 mm thick copper tape. The dielectric insulator was Kapton film tape. Kapton was selected for its electrical properties; a high volume resistivity of $10^{17}\Omega$-cm, high dielectric constant of 2.8, and dielectric strength of 3900 V/mil.

When a sufficiently high voltage a.c. input amplitude is supplied to the electrodes, the air ionizes and forms plasma in the region of largest electric field potential. Since the electrodes are typically long and narrow, the plasma forms at the overlapped edge the upper, exposed electrode and over the lower, insulated electrode. Figure 2.2 shows the glow strip of the plasma actuator.

To create plasma, gas must be ionized, which takes energy. Work must be done to overcome the electrostatic attraction of the electrons to the nucleus. Energetically, the electrons want to recombine with the ions. When the recombination happens, the electron does not return into its original, ground-state orbital. It recombines to a higher, or excited, quantum state, retaining some of the energy it was given when it ionized. These higher energy states are unstable, so the remaining energy is given off as light when the electron drops into the ground state.

The plasma discharge from the actuator is a dielectric barrier discharge with the unique property that it is self-limiting and therefore sustainable at atmospheric pressures [18]. The plasma is formed as the result of a series of discharges as electrons are transferred onto and off of the dielectric insulator. Figure 2.3 shows the electrons emitted from the exposed electrode collect on the dielectric surface of the and are returned on the subsequent half-cycle of the discharge. This build-up of charge on charge on the dielectric surface is the reason that the discharge is self-limiting and does not collapse into a constricted arc.

In the presence of an electric field potential, the ionized air produces a body force on the air [18]. The body force increases with the voltage amplitude in proportion to the volume of plasma (ionized air) and the strength of the electric field gradient. The asymmetric electrode configuration produces a body force that draws ambient fluid toward the wall, and then jets the fluid away from the greatest electric field potential.

When using the actuator, it is useful to understand its operation, and therefore useful to understand how the plasma modifies the electric field that is present when the air between the electrodes is *not* ionized. Charges in a plasma are free to move; therefore, they arrange themselves so as to cancel as much of the field as possible

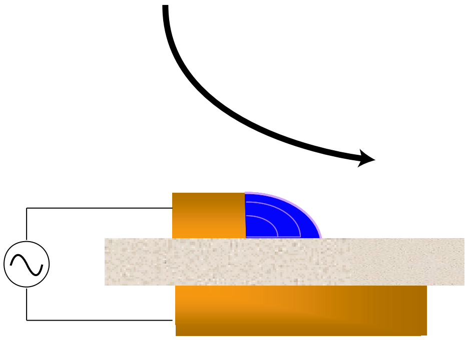

Figure 2.1. Schematic of asymmetric plasma actuators arrangement.

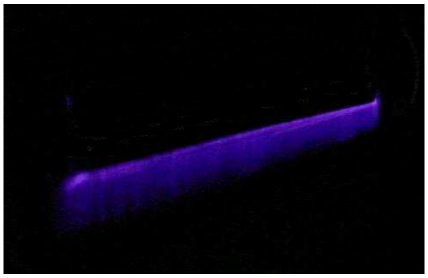

Figure 2.2. Photograph of the plasma actuator, plasma forms at and near the edge of the upper, exposed electrode over the insulated, lower electrode.

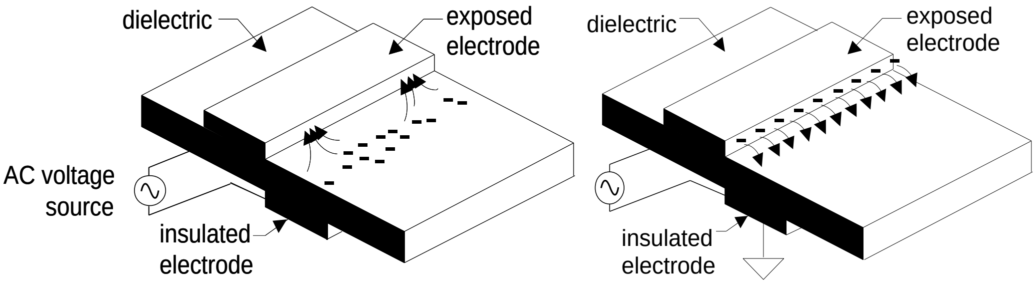

Figure 2.3. Electrons are emitted from the exposed electrode collect on the dielectric surface (left) and are returned on the subsequent half-cycle of the discharge (right). From Enloe, et. al [18].

within the plasma volume. Near the boundaries of the plasma, this is not possible due to the thermal motion of the particles.

Assuming a timescale long enough for the charges to redistribute themselves, the electron density, n_e, and the ion density, n_i, in the plasma can be related to the local electric potential, ϕ, by the Boltzmann relation

$$n_i = n_o \exp\left(-\frac{e\phi}{kT_e}\right) \approx n_o\left(1 - \frac{e\phi}{kT_e}\right) \tag{2.1}$$

$$n_e = n_o \exp\left(\frac{e\phi}{kT_i}\right) \approx n_o\left(1 + \frac{e\phi}{kT_i}\right), \tag{2.2}$$

where n_o is the background plasma density, k is the Boltmann's constant, and T is the temperature. The net charge density, ρ, at any point in the plasma is

$$\rho = e(n_i - n_e) \approx -en_o\left(\frac{e\phi}{kT_i} + \frac{e\phi}{kT_e}\right). \tag{2.3}$$

The electric potential, ϕ, and electric field vector $\vec{E}$ are related through

$$\vec{E} = -\vec{\nabla}\phi. \tag{2.4}$$

From Maxwell's equations and Equation 2.4

$$-\nabla^2\phi = \frac{\rho}{\epsilon_o}, \tag{2.5}$$

where ϵ_o is the permittivity of the free space. Using Equations 2.3 and 2.5

$$\nabla^2\phi = \frac{e^2 n_o}{\epsilon_o}\left(\frac{1}{kT_i} + \frac{1}{kT_e}\right)\phi = \frac{1}{\lambda_D^2}\phi \tag{2.6}$$

where the Debye length, λ_D is defined as

$$\frac{1}{\lambda_D^2} = \frac{e^2 n_o}{\epsilon_o}\left(\frac{1}{kT_i} + \frac{1}{kT_e}\right). \tag{2.7}$$

The Debye length is the characteristic length for electrostatic shielding in a plasma. explain?? From Equations 2.5 and 2.6

$$\rho = -\frac{\epsilon_o}{\lambda_D^2}\phi, \tag{2.8}$$

which says that the net charge density at any point in the plasma is proportional to the potential at that point.

Because there is an electric field in the plasma in regions where there is also a net charge density, there is a force on the plasma. The force density, or body force or force per unit volume, $\frac{\vec{F}_B}{V}$, can be calculated directly by taking the charge density times the electric field strength,

$$\frac{\vec{F}_B}{V} = \rho\vec{E}. \tag{2.9}$$

Since the charge density is proportional to the potential from Equation 2.8,

$$\frac{\vec{F}_B}{V} = \left(\frac{\epsilon_o}{\lambda_D^2}\phi\right)\vec{E}. \tag{2.10}$$

This body force is a vector that can be tailored for a given application through the orientation and design of the electrode geometry.

2.1.2 Electronics

A function generator, amplifiers, and transformers were the main electronic components necessary to generate the plasma. However, high-voltage probes, coil current meters, and oscilloscopes were also utilized to monitor the signals associated with the electronics and the plasma itself. A schematic of the set-up is shown in Figure 2.4. Figure 2.5 is the circuit used to generate the plasma.

A Stanford Research Systems 3.1 MHz function generator was used to supply the 5 kHz driving frequency to generate the plasma. The signal was amplified by a low-power, variable output amplifier, which had a maximum amplification of 10:1 and had the capability of inverting the phase of the signal. Figure 2.6 is a schematic of the circuit of the low-power amplifier. A photograph of the circuit is shown in Figure 2.7.

Further amplification was achieved by using a high-power amplifier (10:1) and a high-voltage transformer (120:1). Figure 2.8 is a schematic of the circuit of the high-power amplifier. It is a linear, Class A, push-pull amplifier. The high-voltage transformer was a custom order from Corona Magnetics in Corona, California. The resulting maximum voltage output of this electronic system is $10 \times 10 \times 120 = 12\,\text{kV}_{p-p}$.

A LeCroy PPE-20kV high-voltage probe was used to monitor the voltage supplied to the electrodes, while a Pearson Model 2100 coil inductance current meter monitored the current. A LeCroy Waverunner LT342 and LT264 was used to monitor the signals to the amplifiers and to the electrodes.

2.1.3 Advantages

Plasma actuators have the potential to produce significant results in the application of flow control. Some of the numerous advantages of the plasma actuators over other flow control devices include:

Fully electronic: The plasma actuators are fully electronic, with no mechanical parts and therefore are able to withstand high force loading.

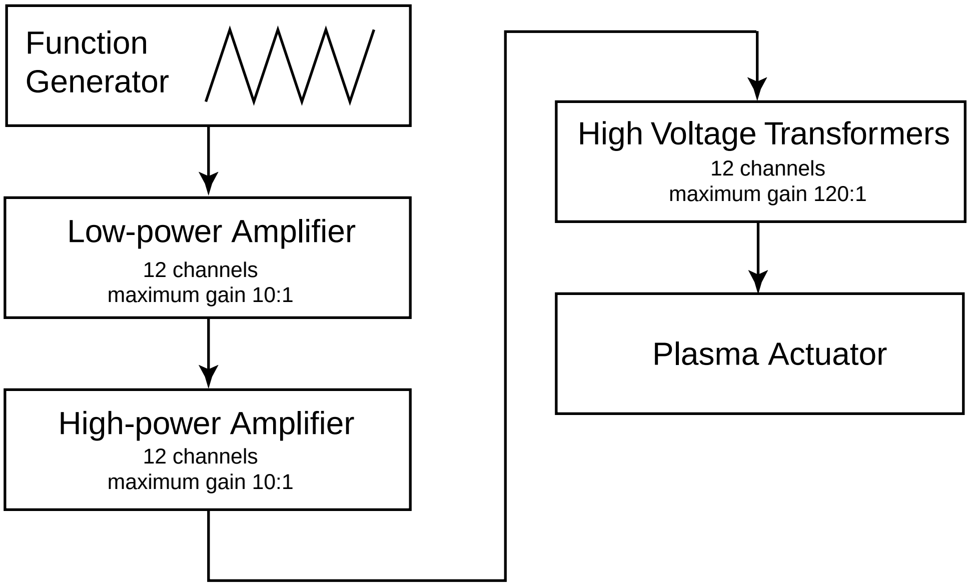

Figure 2.4. Block diagram of the electronic system.

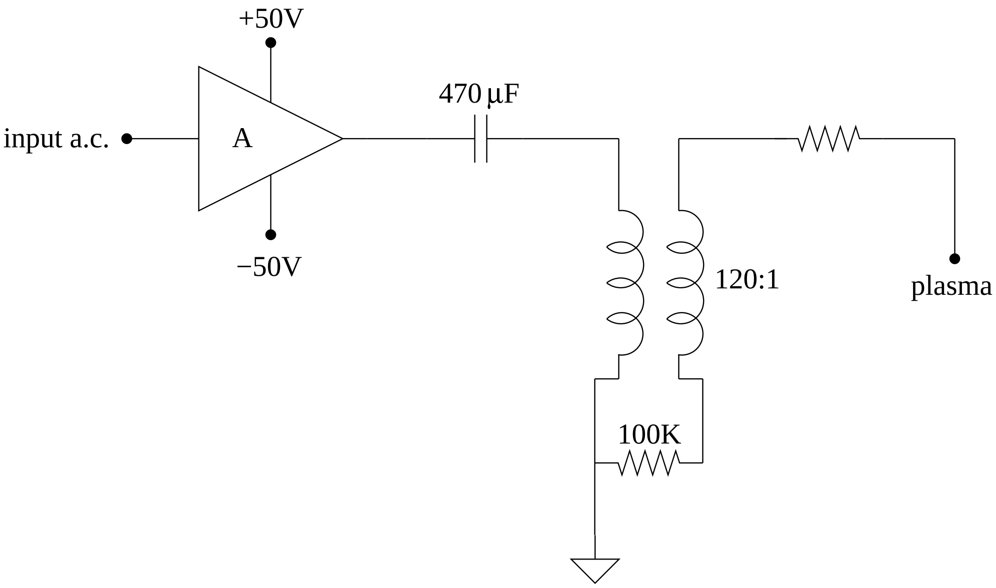

Figure 2.5. Schematic of the circuit used to generate the plasma.

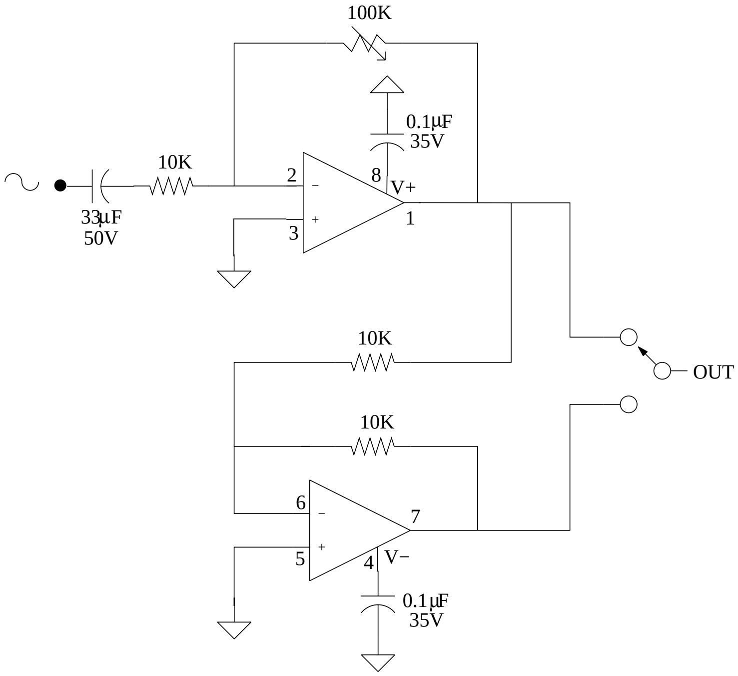

Figure 2.6. Schematic of the low-power amplifier circuit.

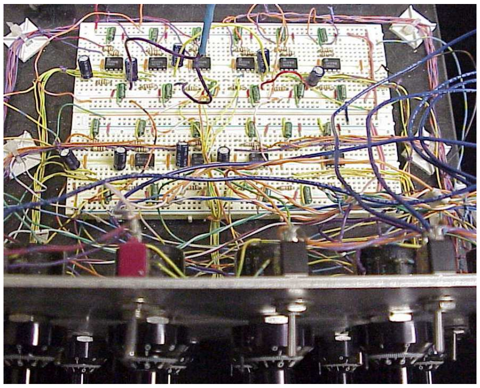

Figure 2.7. Photograph of the low-power amplifier.

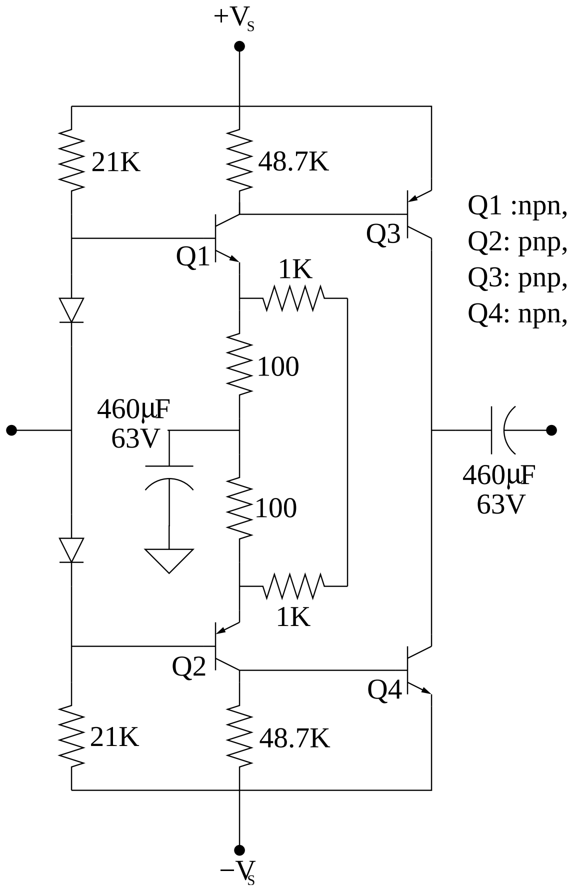

Q1 :npn, 180V, 1.5A, 140MHz, ecg 373
Q2: pnp, 180V, 1.5A, 140MHz, ecg 374
Q3: pnp, 100V, 15A, 140 MHz, ecg 2329
Q4: npn, 100V, 15A, 140 MHz, ecg 2328

Figure 2.8. Schematic of the high-power amplifier circuit.

Scalable in size: Plasma actuators are scalable in size. Electrodes have been constructed as small as 0.5 mm and as large as 20 cm. They also have a low-profile and can be laminated onto wing surfaces, not requiring slots or cavities.

Low mass: The actuator itself is light-weight, which is important where actuation is intended for moving sources.

High-frequency band width: The high-frequency band width allows for fast response for feedback control.

High energy density: The phased plasma are capable of producing large effect with a minimum power input.

2.1.4 Operation

The actuators can be operated either in a "quasi-steady," unsteady, or phased manner. This section explains how each of these can be achieved. In any operation, the operating frequency of the a.c. voltage supplied to the electrodes was typically 5 kHz, and the a.c. voltage supplied to the electrodes was 11 kV$_{p-p}$. The power used by the actuator varied, depending on the mode of operation.

2.1.4.1 Steady Actuation

In the "quasi-steady" manner the input a.c. operating frequency (5 kHz) is well above the fluid response frequency and therefore senses a constant body force. For steady operation, power consumption was estimated to be 20 Watts per foot span. This estimation was based on the measurements from the high-voltage probe and coil current meter.

2.1.4.2 Unsteady Actuation

For unsteady operation of the plasma actuator, the a.c. operating frequency is switched on and off at a lower frequency, which can be down to a fraction of a Hertz. A schematic is shown in Figure 2.9. The unsteady production of the plasma generates unsteady flow disturbances that can be used to excite fluid instabilities which act as a fluid amplifier to produce a larger flow effect.

In this operation, very short duty cycles are possible, which reduce the actuator power significantly. For example, results were obtained with a 10% duty cycle that effectively reduced the power by 90% over the steady operation. Figure 2.10 is a schematic of the circuit used to generate the unsteady signal with variable duty cycle. The LM322 is a precision timer which is used to set the duty cycle. The duty cycle can be precisely adjusted using the variable resistor. The CD4066 is a quad bilateral switch that turns the driving frequency on and off at the unsteady frequency.

2.1.4.3 Phased Actuation

The phased operation requires multiple plasma actuators in aligned in series. The a.c. input to neighboring electrodes are *phase-shifted*, resulting in what appears to be a translating plasma wave.

Figure 2.11 illustrates the concept of phased plasma actuators. The upper electrodes, labeled with (1)'s, are exposed to the air and have a common a.c. supply. The phased electrodes, labeled (2)-(6), are under each upper electrode, yet separated from

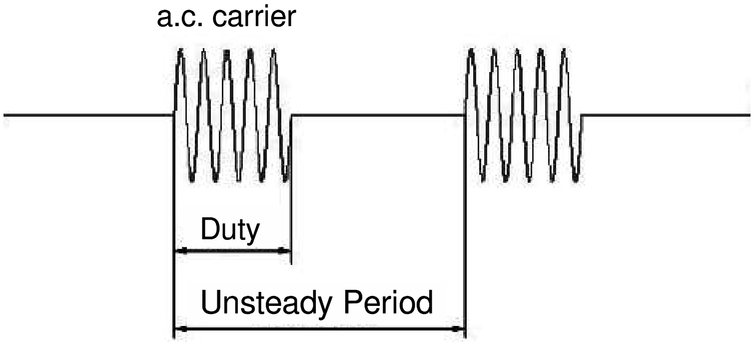

Figure 2.9. Illustration of plasma actuator time series used for unsteady actuation.

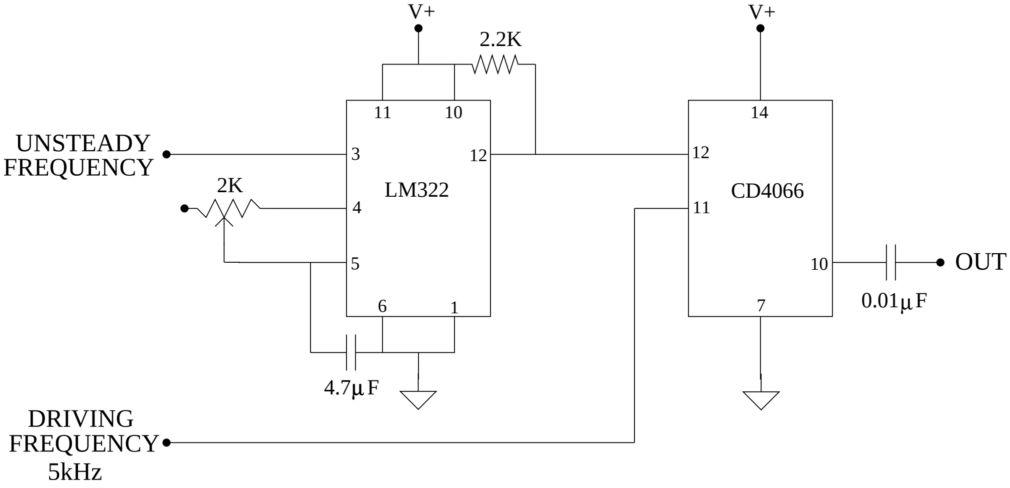

Figure 2.10. Schematic of circuit to generate the signal for the unsteady plasma actuation.

the upper electrodes and each other by a dielectric insulator. The time traces below the electrode pattern depict one complete cycle to each of the electrodes, where the number on the left refers to the particular electrode.

The upper electrodes operate at a short duty cycle time series, with one full period corresponding to τ_2, at a frequency, f_2. For the lower electrodes, the time series is a short duty cycle pulse shifted by an equal amount

$$\text{Phase shift} = \frac{2\pi}{N}. \tag{2.11}$$

In this case, N=5 so the electrodes are phase shifted 72° with respect to each neighboring electrode. The period of that time series is τ_1, where $\tau_1 \neq \tau_2$, at a frequency of f_1.

The plasma forms near the upper electrode exposed to air where the potential is large enough. In Figure 2.11 this occurs where the high and low states of a particular electrode overlap, at electrode (3) and (6). Because the frequencies are different between the time series to the upper and lower electrodes, the location of the plasma moves and the induced velocity and direction of the plasma wave are controlled easily through the frequency difference, $(f_2 - f_1)$.

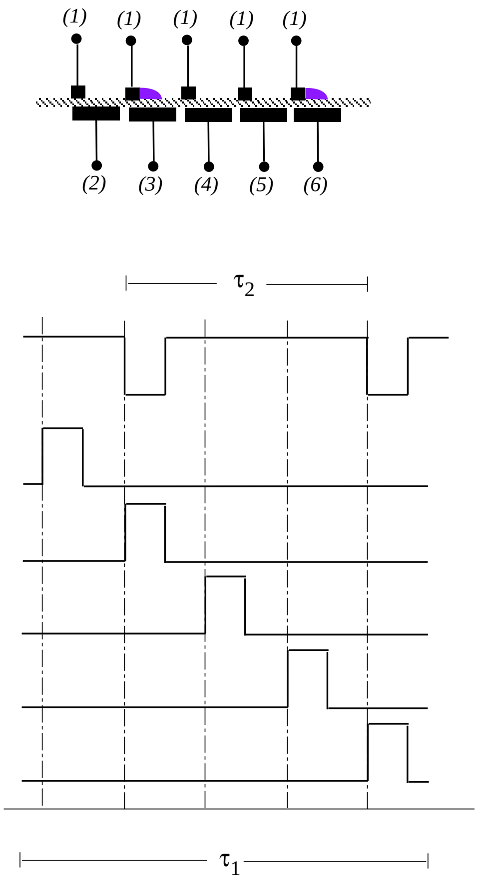

Figure 2.11. Two-frequency phased excitation to produce an uni-direction wave.

2.2 Optimization

The purpose of this work was to fully characterize the plasma actuator through a systematic set of experiments. The focus was on physical actuator configurations, input/output relations, steady versus unsteady actuation, and determining the important time scales associated with the fluid response to the actuator. These experiments were fundamental in optimizing the actuator.

2.2.1 Set-up

Particle Image Velocimetry (PIV) is an experimental technique used to measure the velocity of fluid flows. Since PIV is a non-intrusive measurement technique, it worked well to measure the flow in the vicinity of the plasma where other measurement techniques have failed or have been difficult to obtain accurate measurements.

In the general operation of such a system, the flow is seeded with spherical micro-sized particles. A cross-section of the flow is illuminated using two laser pulses that are temporally separated. The illuminated region is viewed and the light scattered from the particles is captured by a high-resolution camera. A cross-correlation on the two images yields a reconstruction of the flow field.

For this research, a TSI Stereoscopic PIV system was used to obtain instantaneous snapshots of the velocity around the plasma actuator. The flow was seeded by atomized olive oil particles using a Lanskin Nozzle arrangement. The estimated diameter of the particle size was on the order of one micron. The two New Wave Research Nd:Yag lasers operated at 532nm, had a user-defined variable pulse rate,

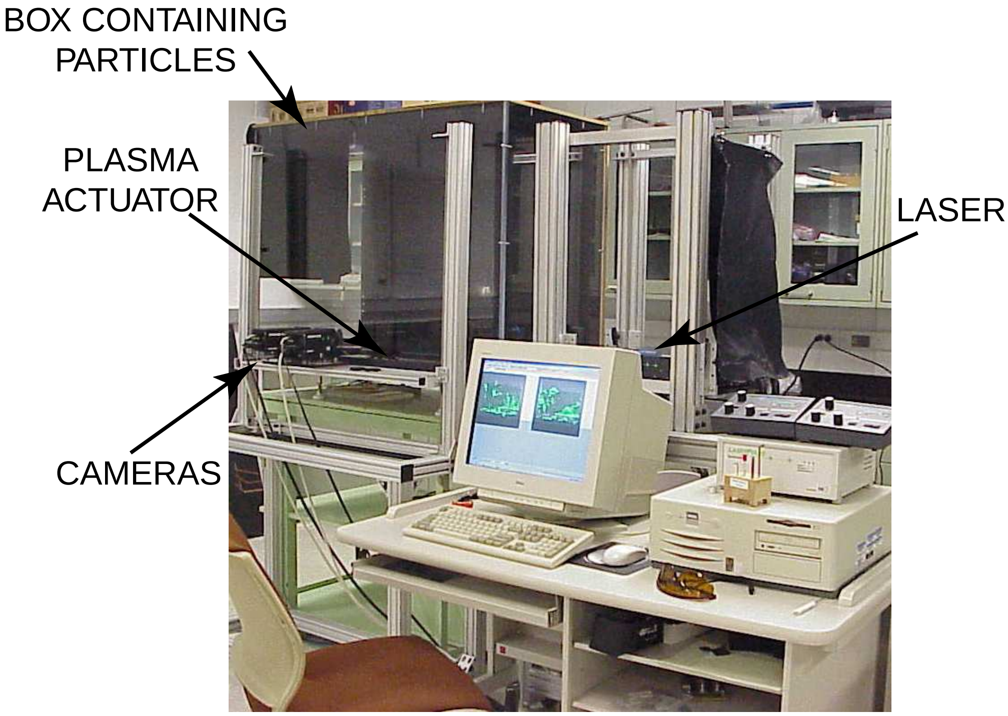

Figure 2.12. Setup of PIV system.

and an energy output of 120mJ per pulse.

The Charged-Coupled Device (CCD) cameras had a 1K by 1K pixel resolution and a frame rate of 30 frames per second. The camera lens was a Nikon 25 mm with a 2x multiplier, which resulted in a resolution approximately of 50 μm per pixel. Sampling was done at 15 Hz.

The study was conducted within the 1.2 m (4 ft) in length by 0.6 m (2 ft) in width by 0.91 m (3 ft) in height box illustrated in Figure 2.12. The front and two sides of the box were made from Plexiglas for laser and optical access. The remaining side, top, and bottom was constructed of particle board for strength. The still, ambient air and atomized olive oil particulates inside the box was unaffected by typical air disturbances, ie. ventilation or fans. Therefore, the measurements of the velocity within the box provided a direct measure of the transport of the particles due to the plasma actuator.

The asymmetric plasma actuator was constructed from 2 mil thick copper tape and 6 mil of Kapton dielectric insulator. The electrodes were 16 mm in width and 13.5 mm in length. Overlap of the upper electrode onto the lower electrode was on the order of 1 mm. The voltage supplied to the electrodes was monitored by a LeCroy PPE-20kV high-voltage probe. The current was measured by a Pearson Model 2100 coil inductance current meter. Both signals were displayed and averaged on a LeCroy LT342 or LT264 oscilloscope.

2.2.2 Steady Actuator

The single plasma actuator was the most basic configuration and was investigated first. The lower electrode was 16 mm in width and 12.5 mm in length. A dielectric layer of 6-mil thick Kapton film insulated the lower electrode from the upper electrode and the air. The upper, exposed electrode was 2 mm wide and overlapped the lower, insulated electrode by 1 mm. PIV data was taken at the mid-span location and the flow induced by the actuator was assumed to be two-dimensional.

Both steady and unsteady operation of the plasma actuator were investigated. Results in this section look at the maximum velocity output of the actuator while varying several parameters. The maximum velocity generated by the plasma actuator was determined from an ensemble average of 100 instant realizations. The driving frequency of the actuator was 5 kHz triangle waveform in all cases, unless otherwise noted. Figure 2.13 shows ensemble-average PIV velocity vectors for a single, steady actuator. The actuator is located at $x = 0\,\mathrm{mm}$ and generates a body force in the positive x-direction.

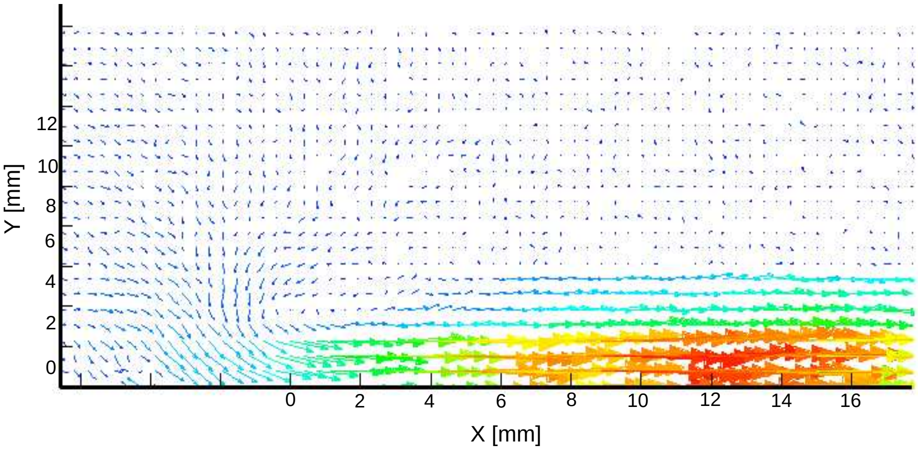

Figure 2.13. PIV velocity vectors of a single, steady actuator).

2.2.2.1 Single Steady Actuator

The results presented here detail the actuator input/velocity output relationship, the independency of waveform input on output, the slight dependency of operating frequency on output, the near linear dependency of power on output, and the dependency of lower electrode width on output.

Effect of Amplitude Input

To accurately model the plasma actuator, a relationship between actuator voltage amplitude input and maximum velocity output was established. The voltage was increased in $2\,\mathrm{kV}_{p-p}$ increments up to $16\,\mathrm{kV}_{p-p}$. Figure 2.14 shows the peak velocity versus input voltage. The maximum velocity output is a function of the actuator voltage amplitude and is related by

$$U = 0.0018V^{7/2}. \tag{2.12}$$

This result is consistent with the numerical simulations of a lumped-element circuit model of the plasma actuator by Enloe, et.al [18], who determined a relation of the power dissipated in the plasma as $V^{7/2}$. For comparison purpose, the curve $U = 0.0344V^2$ is also plotted.

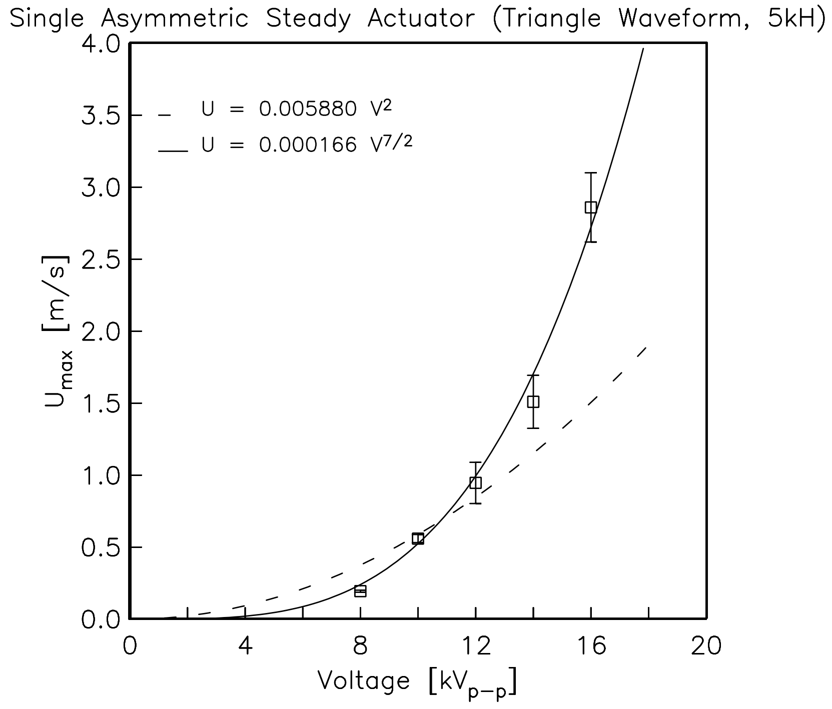

Figure 2.14. Relationship between actuator voltage amplitude input and velocity output for a single steady actuator (Triangle Waveform, Operating frequency: 5 kHz).

Effect of Waveform Inputs

Figure 2.15 shows the maximum velocity of a single, steady plasma actuator generated with different driving waveforms. The driving frequency of the actuator was 5 kHz and the voltage amplitude to the actuators was 12 kV$_{p-p}$. The square, triangle, and sawtooth waveforms appear to have little effect on the maximum velocity output of the actuator. These results are inconsistent with these of Enloe, et.al [18], who found the positive-slope sawtooth waveform to generate more thrust that the other waveforms.

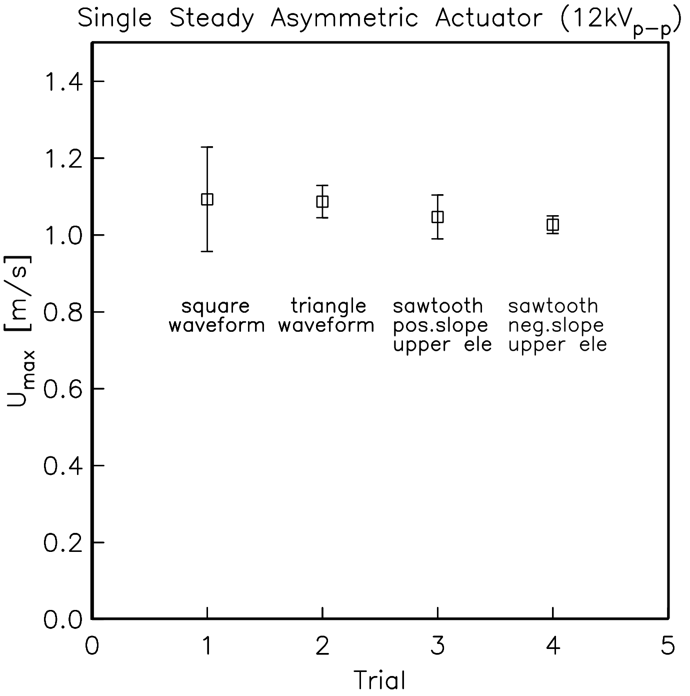

Figure 2.15. Comparison of maximum velocity output for various driving waveforms.

Effect of Operating Frequency and Power

The driving frequency of the plasma was varied from 2 kHz to 10 kHz, in 1 kHz increments. The maximum velocity output and power used versus the driving frequency is presented in Figure 2.16. Evident is a linear relationship between driving frequency and power. As the driving frequency increases, the power necessary to generate the plasma at a constant 12 kV$_{p-p}$ also increases. However, the maximum velocity generated by the plasma increases until it asymptotes at about 1.3 m/s. This means that there may be some optimal driving frequency for maximizing the velocity output and minimizing the power consumption for steady plasma actuation. All of the data presented in this research was collected at a driving frequency of 5 kHz, which was considered optimal for the plasma generating electronics.

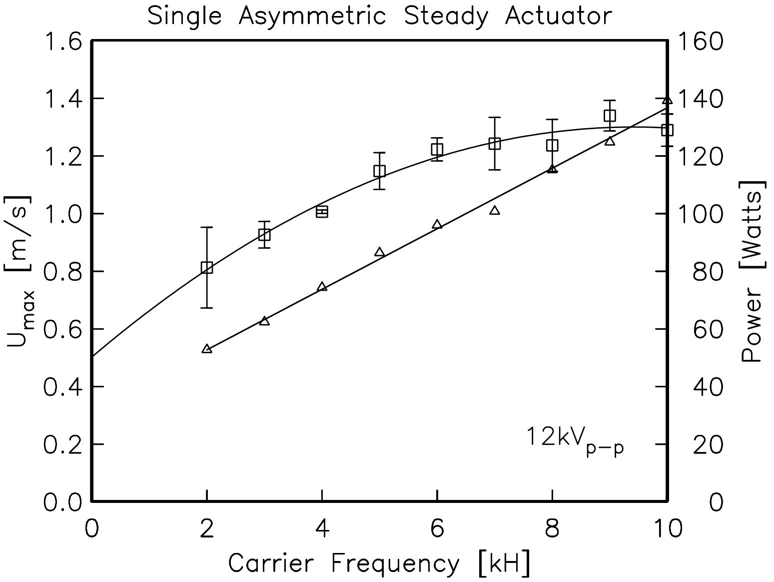

Figure 2.16. Comparison of velocity output and power for different driving frequencies.

Effect of Width of Lower Electrode

When designing the physical electrode arrangement, the lower, insulated electrode should be sufficiently wide to allow for the plasma form and upper, exposed electrode needs to be wide enough so that plasma does not form on both of its edges. Figure 2.17 assigns a numerical value to how wide the lower, insulated electrode should be to use the full potential of the plasma. The lower, insulated electrode width was varied for two constant voltage input cases, $12\,\mathrm{kV}_{p-p}$ and $16\,\mathrm{kV}_{p-p}$. The results indicate that the maximum velocity generated by the actuator increases as electrode width increases, until it asymptotically approaches its maximum value. This maximum velocity is then a function of the voltage input amplitude and a *sufficiently* wide lower electrode.

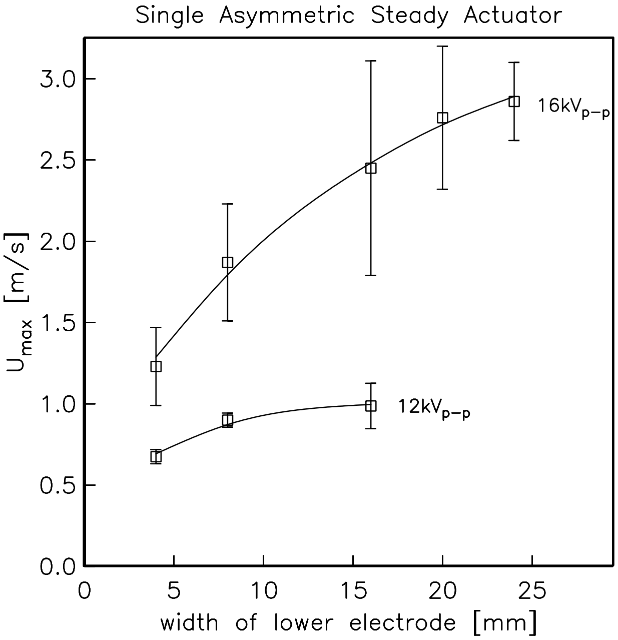

Figure 2.17. Maximum velocity versus width of lower electrode.

2.2.2.2 Multiple Steady Actuators

The lower electrodes were 8 mm in width and 12.5 mm in length and were separated by a 4 mm gap. The total width of lower electrodes (8 mm + 8 mm) was kept the same as the single, steady actuator case of 16 mm. A dielectric layer of 6-mil thick Kapton film insulated the lower electrodes from the upper electrodes and the air. The upper, exposed electrodes were 2 mm wide and overlapped the lower electrodes by 1 mm.

Figure 2.18 shows the maximum velocity output generated by one and two steady plasma actuators. The trend remains $V^{7/2}$ as with the single actuator case, but the leading coefficient has doubled. This is an important result because it means that the maximum velocity output of the actuator is additive.???

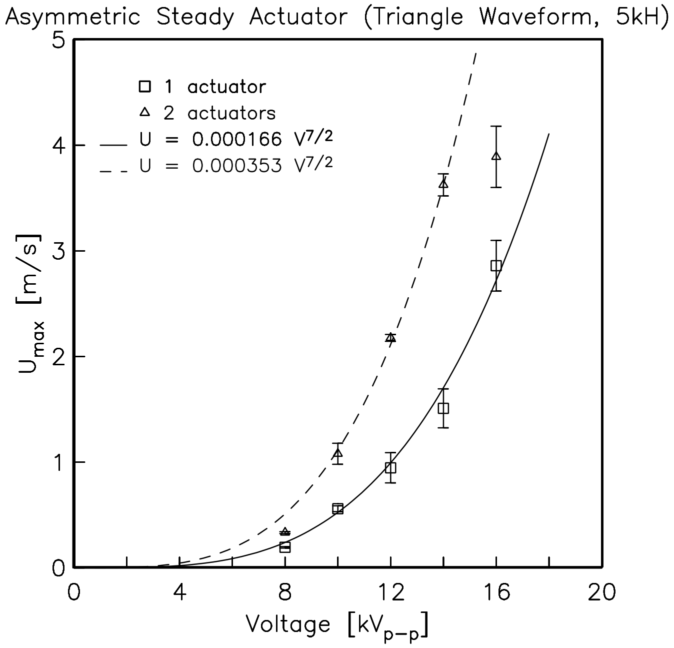

Figure 2.18. Relationship between actuator voltage amplitude voltage input and velocity output for one and two steady actuators (Triangle Waveform, Operating frequency: 5 kHz).

2.2.3 Unsteady Actuator

The velocity output normalized by the maximum velocity output of a single, steady plasma actuator versus time is shown in Figure 2.19. To obtain this data, phased-averaged velocity vectors at different phases in a low frequency (0.5 Hz) unsteady cycle.

Figure 2.20 shows phase-average velocity vectors at different phases of the 0.5 Hz cycle. Each of the six plots are a result of an ensemble average of 100 instant realizations. At 2 ms as the plasma first initiates, the velocity vectors show the initial entrainment of air near the actuator. A vortex has clearly formed at 12 ms and is convected to the right.

When the plasma first initiates each time in the cycle, the result is similar to that of an impulsively moved wall; the formation of a starting vortex. The premise is that once formed, the starting vortex has a fixed convection velocity that is the same as the maximum velocity of the case of the steady actuator.

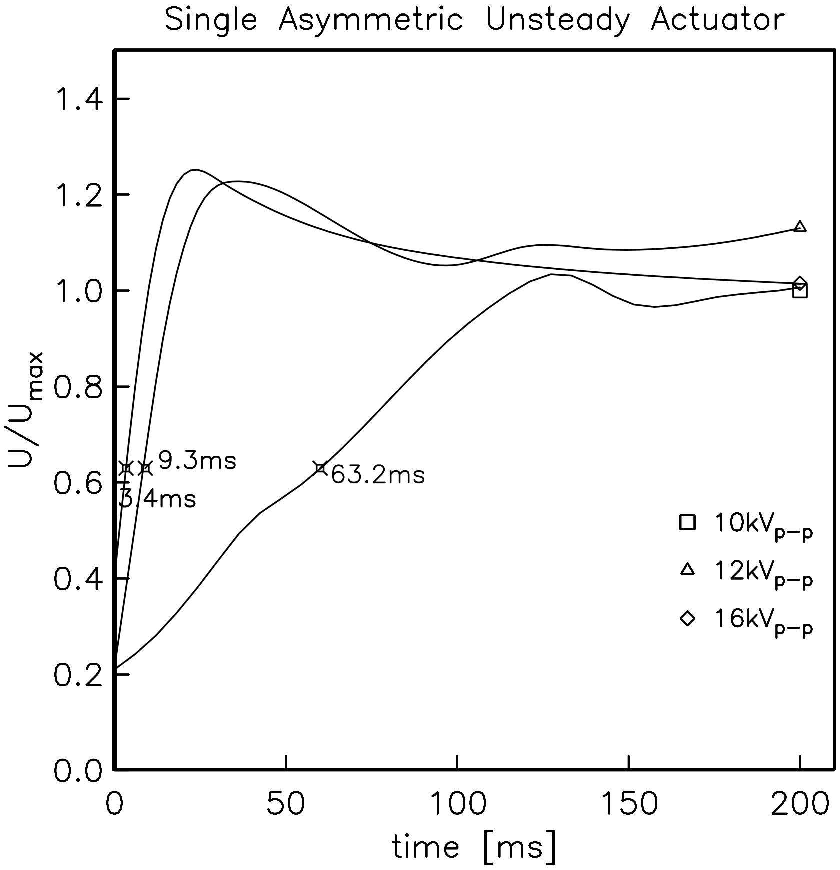

Figure 2.19. Time constants for different voltage amplitudes for a single, unsteady plasma actuator (Triangle Waveform, Operating frequency: 5 kHz).

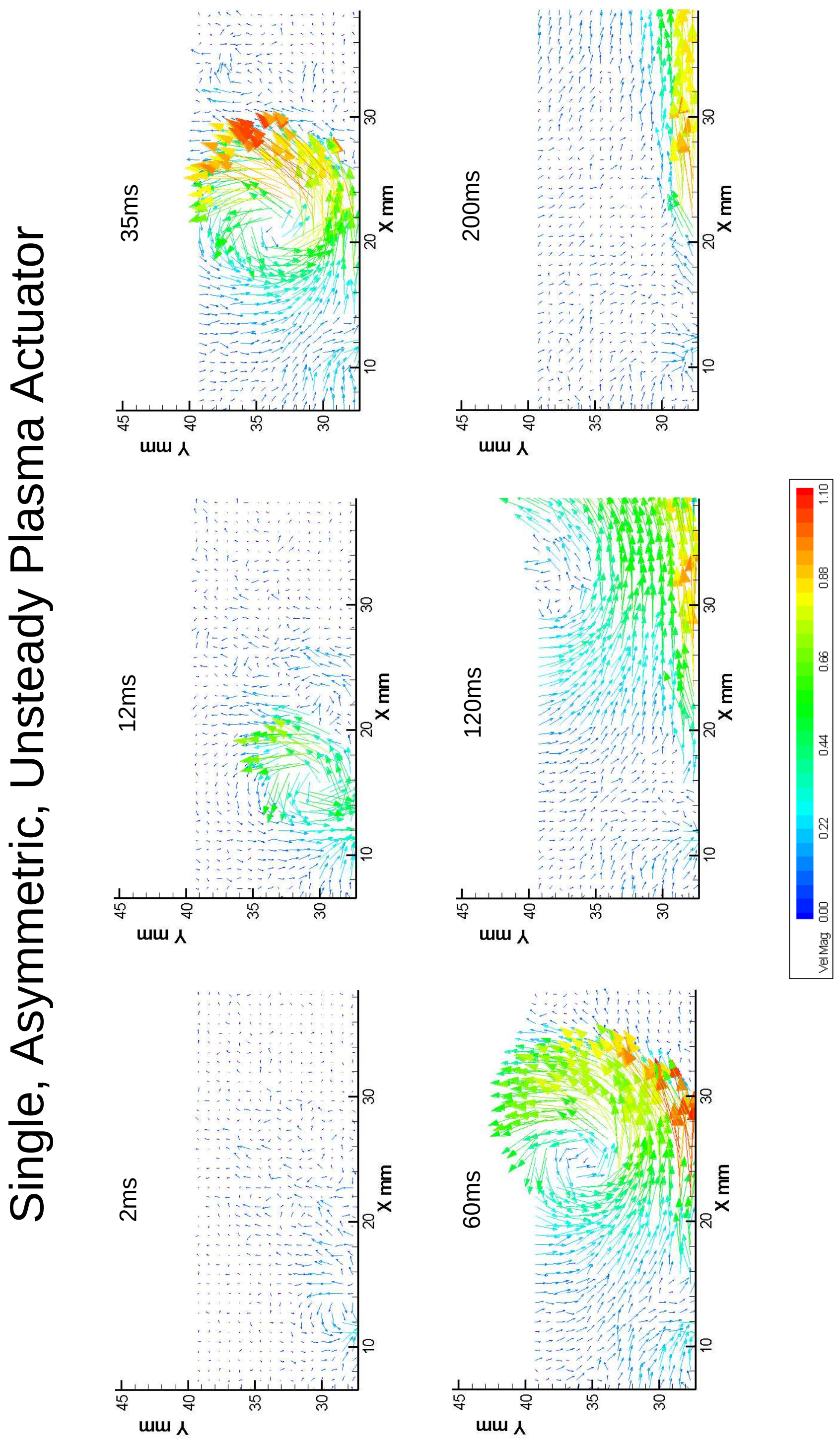

Figure 2.20. Phase-averaged velocity vectors at different phases of the 0.5 Hz unsteady plasma actuator cycle.

2.2.4 Phased Actuator

The a.c. frequency supplied to the two electrodes was on the order of 5 kHz, but differed by $\Delta f = f_1 - f_2$. As a result of this frequency difference, the intensity of the plasma increased and decreased with the period Δf.

To obtain the data for the phased actuator, a phase-locked trigger signal, needed as a reference signal to trigger PIV system at any desired time in the periodic plasma cycle, was constructed from the two a.c. signals supplied to the electrodes. Figure 2.21 is a box diagram and Figure 2.22 is an electrical schematic of the method used to construct the trigger signal for the PIV system for phased-averaged velocity measurements.

The signals were fed through an analog multiplier to form a new time series with frequencies at $f_1 \pm f_2$. A low-pass filter was used to retain the lower, difference component of the time series. The remaining time series was converted to a TTL pulse series, which was used as a phase reference for triggering the PIV system. The PIV software allows for a variable delay with respect to the phase-locked trigger signal, so that data can be acquired at any time within the plasma cycle.

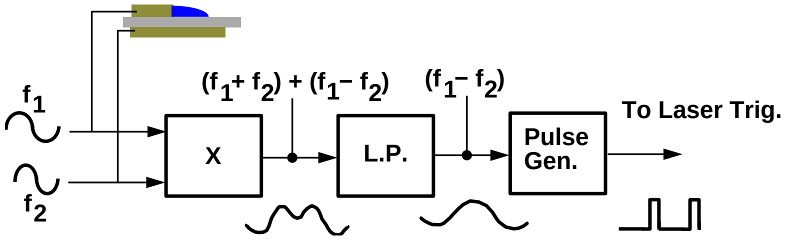

Figure 2.21. Box diagram of the method used to generate the PIV trigger signal.

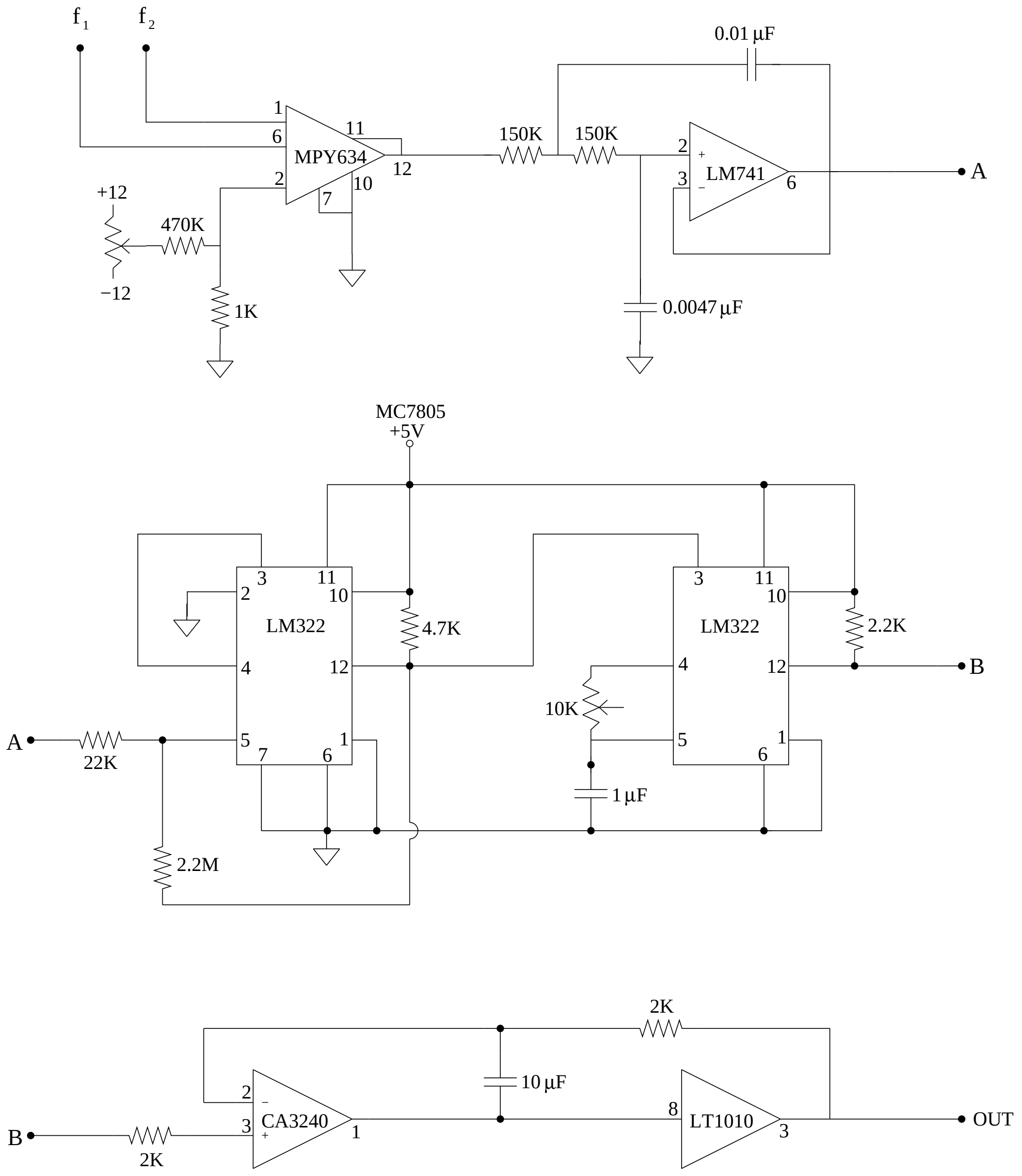

Figure 2.22. Schematic of the circuit used to generate a reference signal to trigger the PIV system at any time in the phased plasma cycle.

Like in the unsteady operation of the plasma, as the plasma first initiates each time in the phased cycle, a starting vortex is formed. To demonstrate that the starting vortex, once formed, has a fixed convection velocity, phase-averaged velocity vectors were acquired for three different actuator frequencies of 1, 2, and 5 Hz, as shown in Figure 2.23. In all three plots, the phase of the trigger in the cycle of the plasma actuator was kept fixed.

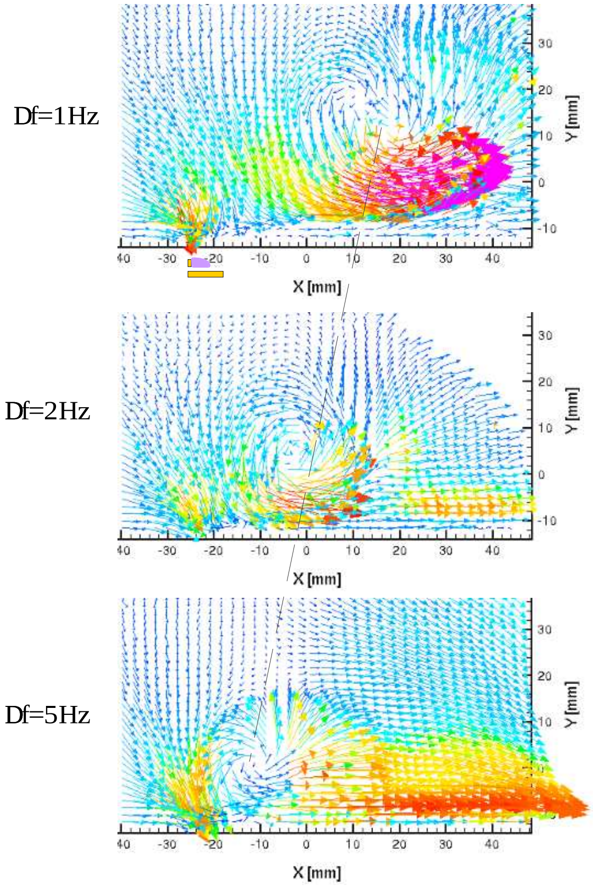

Figure 2.23. Phase-averaged velocity vectors at the same phase trigger, at different frequencies of the plasma actuator.

CHAPTER 3

EXPERIMENTAL SETUP

3.1 General

3.1.1 Experimental Facility

The experiments were conducted in one of the subsonic wind tunnels in the Center for Flow Physics and Control (FlowPAC) in the Hessert Laboratory at the University of Notre Dame. The facility is an open-return wind tunnel with a 0.61 m by 0.61 m (2 ft square) by 1.8 m (6 ft) long test section. The tunnel consists of a removable inlet having a series of 12 screens followed by an 18:1 contraction that attaches to the test section. The test section is equipped with a Plexiglas wall and a glass floor that allow optical access when flow visualization is performed. The back wall of the test section was used to mount the airfoil. Removable hatch doors in the back wall provided access into the test section. In addition, a slot in the test section ceiling provided access for a probe connected to a motorized traverse system. A schematic of the wind tunnel is shown in Figure 3.1, and a photograph of the facility is illustrated in Figure 3.2.

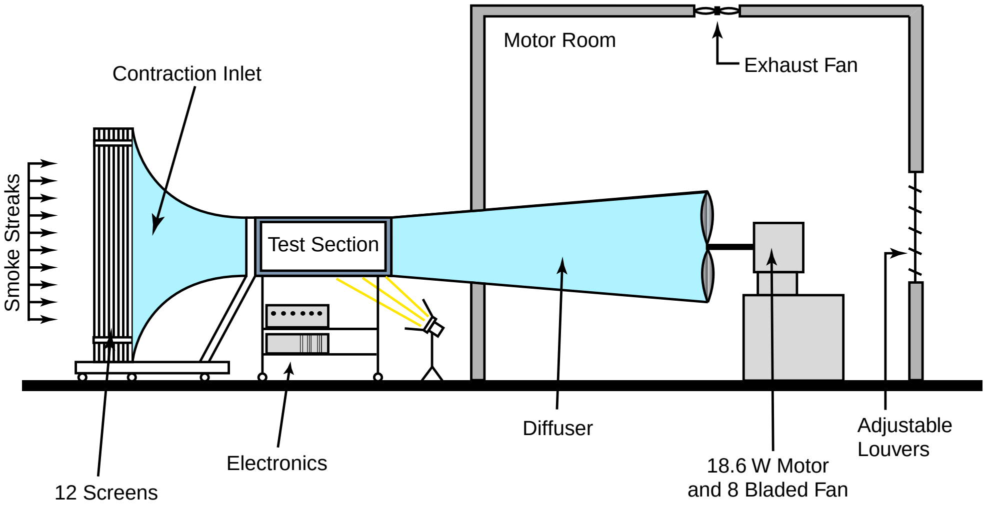

Figure 3.1. Schematic of the open-return wind tunnel at the Center for Flow Physics and Control.

Figure 3.2. Photograph of experimental facility.

3.1.2 Flow Visualization

Flow visualization was done by introducing continuous smoke streaklines upstream of the wind tunnel screens and contraction. The smoke generator was originally built by Brown in 1937 at the University of Notre Dame. A description is given by Mueller [57]. The smoke emanated from a rake of tubes as low-speed laminar jets. The tubes were aligned in the vertical direction and located at the spanwise centerline. The smoke streaks were drawn into the tunnel inlet and converged into a closely spaced, vertically aligned group following the contraction. Figure 3.3 shows the smoke generator and close-up photograph of the smoke rake upstream of the contraction of the open-return wind tunnel at the Center for Flow Physics and Control.

For the case of the stationary airfoil, the smoke streaks were illuminated by a steady, high-intensity light source located below the tunnel test section. For the oscillating airfoil, a strobe light source was used. It was externally triggered by the motor encoder output at specific airfoil angles to obtain phase-conditioned visualization records. In both cases, the light entered through a glass slot in the floor of the test section. Most flow visualization results in this dissertation have been mirrored about the x-axis to show a positive angle of attack.

The flow visualization records were made using a Panasonic analog video camera. The video tape was digitized through a video capture card where individual frames were extracted. An example of a flow visualization image is shown in Figure 3.4. In this arrangement, flow visualization was possible for freestream speeds up to 30 m/s.

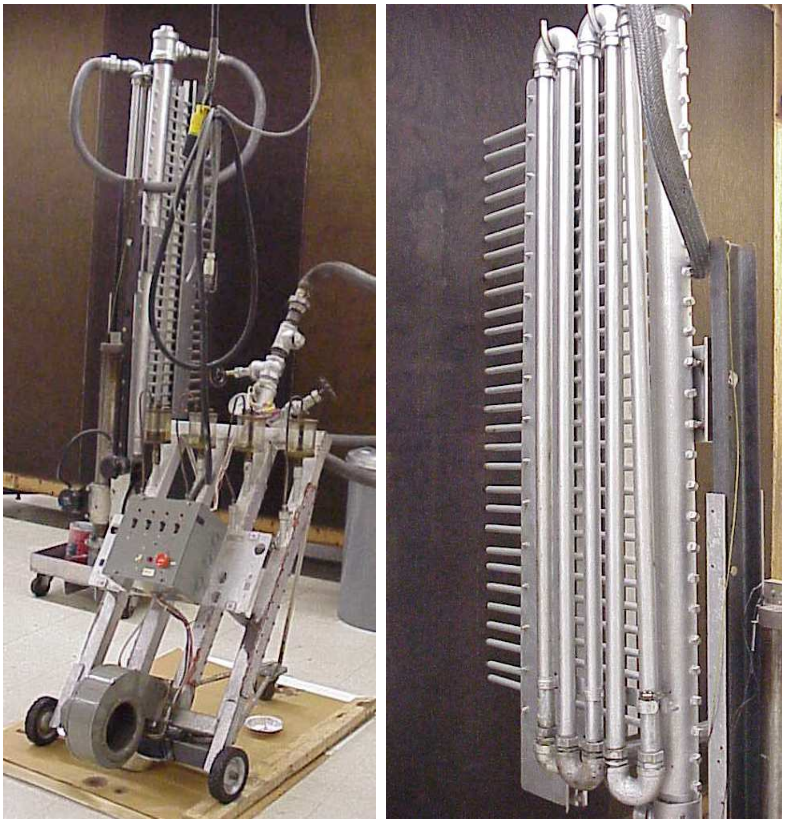

Figure 3.3. Photograph of the smoke generator and close-up of the smoke rake at the Center for Flow Physics and Control.

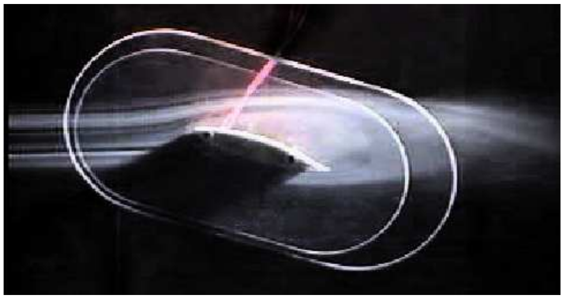

Figure 3.4. Sample flow visualization image for the NACA $66_3 - 018$ airfoil at 16° angle of attack and a freestream velocity of 20 m/s (65.9 f/s).

3.2 Stationary

3.2.1 Airfoil

Two symmetric airfoils were used in the stationary airfoil study: NACA $66_3 - 018$ and NACA 0015. The shapes were chosen because the steady characteristics of these airfoils are well-known and documented in the literature [1], and both exhibit leading-edge separation.

The NACA $66_3 - 018$ was chosen because it had been previously used at Notre Dame with lift-drag measurements performed using a drag balance. These previous measurements were used to make a direct comparison to benchmark lift and drag inferred from surface pressure measurements and wake profiles. The NACA 0015 was chosen because it had been commonly used for helicopter rotor blades and numerous experimental results exist in the literature [1, 5, 32, 43, 48, 77].

Both airfoils had a 12.7 cm (5 in) chord and a 25.4 cm (10 in) span. The size of the airfoils was set so as to minimize blockage effects, especially at the large angles of attack that were investigated. They were cast in an epoxy-based polymer in a two-piece aluminum mold. The mold used to cast the NACA 0015 airfoil is shown in Figure 3.5. It was precisely machined using a numerical-controlled milling machine. The locations of surface pressure ports were drilled as holes in the surface of the mold. These accepted tubulations, 0.5 mm (0.02 in) I.D., that were cast into the airfoil and brought out through a hollow tube support on one end of the model. After the casting material had hardened, the airfoil was released from the mold and the pressure tubing projections were trimmed flush with the airfoil surface.

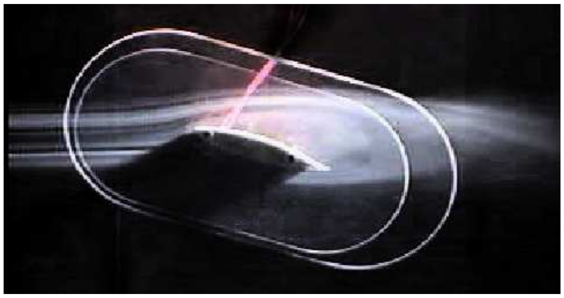

Figure 3.5. Aluminum mold used to cast the NACA 0015 airfoil.

End plates were used to minimize 3-D end effects on the airfoils. The end plates were constructed from clear Plexiglas to allow visual access for flow visualization over the surface of the airfoil. The end plates were 40.6 cm (16 in) by 20.2 cm (8 in), with a 10.2 cm (4 in) radius and were 3.2 mm (0.125 in) thick. A schematic drawing of the NACA 66_3-018 airfoil and a photograph outside the tunnel test section is shown in Figure 3.6.

The airfoils were mounted by passing the support tube through the back wall of the test section. The tube was held in place by a chuck that allowed angular motion for setting the angle of attack. The pressure tubes exited the tunnel through the support tube.

The plasma actuator consisted of two copper electrodes separated by a 5-mil thick Kapton film. The electrodes were made from 0.0254 mm thick copper foil tape, which was bonded directly to the surface of the airfoil. It filled a recess to produce a smooth, flush surface with the airfoil shape. Two actuators were used on the NACA 66_3-018 airfoil. One was placed precisely at the leading edge ($x/c = 0$), and oriented to produce a velocity component toward the suction side of the airfoil when at an angle

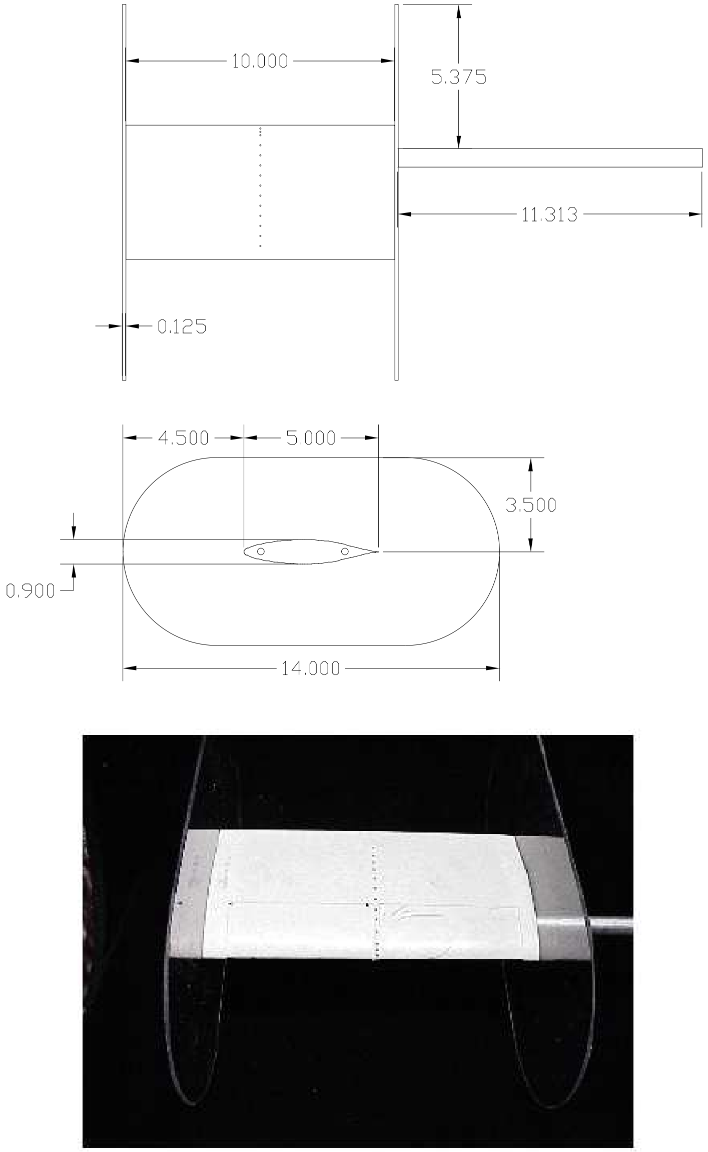

Figure 3.6. Schematic drawing and photograph the NACA 66_3-018 airfoil with end plates. Dimensions are in inches.

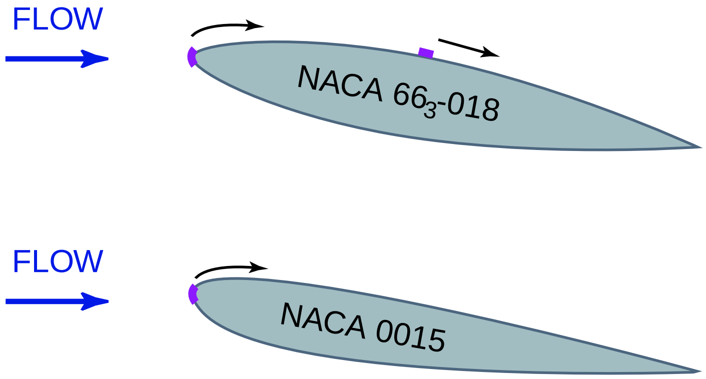

Figure 3.7. Schematic drawing showing the locations and orientations of plasma actuators used for separation control on and NACA $66_3 - 018$ and NACA 0015.

of attack. The other was placed near the maximum thickness location ($x/c = 0.5$), and oriented to produce a velocity component in the mean freestream direction.

A single actuator was used on the NACA 0015. It was placed at the leading edge ($x/c = 0$), and oriented to produce a velocity component toward the suction side of the airfoil when at an angle of attack. The actuator placement on the two airfoils is illustrated schematically in Figure 3.7.

Photographs of the NACA airfoil with the electrodes and Kapton film in place are shown in Figure 3.8. The space that was allotted for the actuator on the airfoil was relatively large to accommodate a variety of configurations. In the top photograph, most of the area is passive and covered by Kapton film to bring the recessed area flush with the other airfoil surface. The active actuator regions are best seen in the lower photograph which shows the two lines of plasma that are weakly visible at the leading edge and mid-chord locations when viewed in a darkened lab. The actuator spanned most of the width of the airfoil. A narrow gap was left at the location of the pressure taps, although both sides were electrically connected together.

Photographs of the NACA $66_3 - 018$ airfoil with the electrodes and Kapton film in place are shown in Figure 3.8. The space that was allotted for the actuator on the airfoil was relatively large to accommodate a variety of configurations. In the top photograph, most of the area is passive and covered by Kapton film to bring the recessed area flush with the other airfoil surface. The active actuator regions are best seen in the lower photograph which shows the two lines of plasma that are weakly visible at the leading edge and mid-chord locations when viewed in a darkened lab. The actuator spanned most of the width of the airfoil. A narrow gap was left at the location of the pressure taps, although both sides were electrically connected together.

The operating frequency of the a.c. voltage supplied to the electrodes was typically 5 kHz. The a.c. voltage supplied to the electrodes was 11 kV_{p-p}, unless otherwise specified.

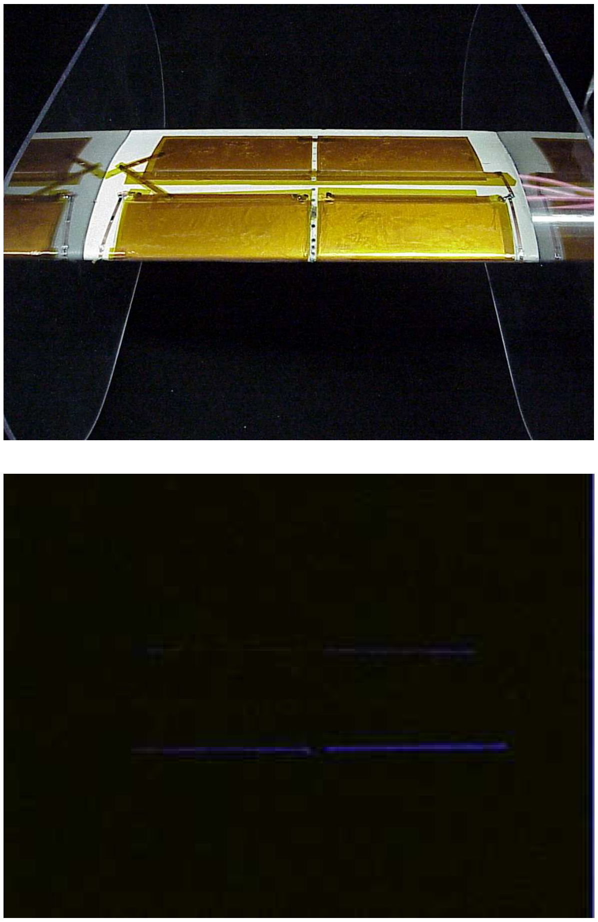

Figure 3.8. Photographs of the $NACA66_3 - 018$ airfoil with plasma actuators at the leading edge and mid-chord locations (top) and lines of plasma when viewed in a darkened lab (bottom).

3.2.2 Pressure Data Acquisition

A total of 29 surface pressure ports, 0.5 mm (0.02 in) I.D., were aligned with the flow direction at the half-span location on the airfoil. Although they were spaced relatively uniformly around the airfoil, there was a slight increase in concentration of ports near the leading edge. Table 3.1 provides the positions of the surface pressure ports.

Table 3.1. Static pressure port locations on the surface of the stationary airfoil.

Port #	x/c	Port #	x/c
0	0.0		
1/2	0.025	15/16	0.0456
3/4	0.051	17/18	0.532
5/6	0.076	19/20	0.608
7/8	0.152	21/22	0.684
9/10	0.228	23/24	0.759
11/12	0.304	25/26	0.835
13/14	0.380	27/28	0.911

The pressure measurements were made utilizing a Scanivalve Model J9 scanning pressure valve. A Validyne DP103 pressure transducer, with range up to 5.5 in. $\mathrm{H_2O}$, and CD23 carrier demodulator was used to capture the pressure measurements. It was selected because of its stability and low frequency response. Static calibration of the pressure transducer was performed by connecting the pitot static probe in the freestream in parallel with a calibrated pressure transducer. Velocities were varied in the range of 0 to 35 m/s. The carrier demodulator was adjusted to provide a gain of 5, resulting in a calibration coefficient of 1.85 volts/ in. H_2O, as shown in Figure 3.9.

For wind tunnel operations, a pitot static probe located in the freesteam provided the reference static pressure for each pressure port. A second pitot static probe was

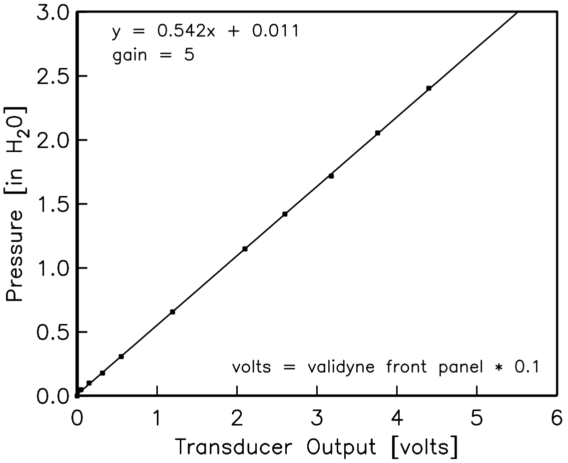

Figure 3.9. Static calibration curve for the Validyne pressure transducer.

mounted to a traversing mechanism two chord lengths downstream of the airfoil in its spanwise centerline. Discrete points were sampled across the wake to construct the mean velocity profile.

On the surface of the airfoil, the coefficient of pressure, C_p, was calculated as

$$C_p = \frac{P_s - P_\infty}{\frac{1}{2}\rho U_\infty^2} = \frac{P_s - P_\infty}{P_0 - P_\infty} \tag{3.1}$$

where P_s is the static pressure at each port, P_∞ is the static pressure of the freestream, ρ is the density of the freestream air, U_∞ is the velocity of the freestream, and P_0 is the total pressure of the freestream.

The coefficient of lift, C_l, was found by integrating the C_p distribution around the airfoil. Since high angles of attack were investigated with the oscillating airfoil, the coefficient of lift was calculated using

$$C_l = C_n \cos\alpha - C_a \sin\alpha \tag{3.2}$$

where c_n is the normal force coefficient given by

$$C_n = \int_0^1 (C_p^L - C_p^U) d\left(\frac{x}{c}\right) \tag{3.3}$$

and c_a is the axial force coefficient given by

$$C_a = \int_0^1 \left(C_p^U \left(\frac{dy_U}{c}\right) - C_p^L \left(\frac{dy_L}{c}\right)\right) d\left(\frac{x}{c}\right), \tag{3.4}$$

where the subscripts and superscripts of U and L refer to the upper and lower surface of the airfoil, respectfully.

The drag coefficient, C_d, on the airfoil was determined from the mean velocity profiles taken in the wake. This is given as

$$C_d = \frac{4}{U_\infty^2} \int_0^1 U(y)(U_\infty - U(y)) d\left(\frac{y}{H}\right) \tag{3.5}$$

where $U(y)$ is the local mean streamwise velocity, and H is a distance which encompasses the full wake. The velocity profiles used to determine the drag were measured well downstream of any recirculation region that might exist in the separated flow at high angles of attack. This location was two chord lengths downstream of the trailing edge.

Data acquisition was performed using a LabView program. The surface pressure measurements were scanned separately at each port. The velocity profile in the wake scanned starting from the bottom of the wake up to the top of the wake in 0.3175 cm (0.125 in) increments.

Data processing was done using Matlab. A program was written to calculate the coefficients of lift and drag using the previously given definitions.

3.3 Oscillating

3.3.1 Airfoil

A NACA 0015 airfoil was used in this study. It was chosen because the characteristics of this airfoils is well-known and documented in the literature, and both exhibit leading-edge separation. The NACA 0015 was also chosen because it had been commonly used for helicopter rotor blades and several experimental results for oscillating conditions exist for it in the literature [1, 5, 32, 43, 48, 77].

The airfoil had a 12.7 cm (5 in) chord and a 25.4 cm (10 in) span. The size of the airfoil was set so as to minimize blockage effects, especially at the large angles of attack that were investigated. It were cast in an epoxy-based polymer in a two-piece mold. The mold was precisely machined using a numerical-controlled milling machine. The locations of surface pressure ports were drilled as holes in the surface of the mold. These accepted tubulations, 0.5 mm (0.02 in) I.D., were cast into the airfoil and brought out through a hollow tube support on one end of the model. After the casting material had hardened, the airfoil was released from the mold and the pressure tubing projections were trimmed flush with the airfoil surface.

End plates were used to minimize 3-D end effects on the airfoils. The end plates were constructed from clear Plexiglas to allow visual access for flow visualization over the surface of the airfoil. The end plates were round, with a 40 cm (15.75 in) diameter and were 3.2 mm (0.125 in) thick. The center of the circular end plates was at the airfoil's pitch location, which corresponded to the quarter-chord location. With this configuration, the end plates appeared stationary in the flow visualization results.

A schematic drawing of the airfoil with circular endplates and a photograph inside the test section in shown in Figure 3.10. The airfoils were mounted by passing the support tube through the back wall of the test section. The pressure tubes exited the tunnel through the support tube.

The plasma actuator consisted of two copper electrodes separated by a 5-mil thick Kapton film. The electrodes were made from 0.0254 mm thick copper foil tape, which was bonded directly to the surface of the airfoil. It filled a recess to produce a smooth, flush surface with the airfoil shape. A single actuator was used on the NACA 0015. It was placed at the leading edge ($x/c = 0$), and oriented to produce a velocity component toward the suction side of the airfoil when at an angle of attack. The two airfoils the actuator placement is illustrated schematically in Figure 3.11.

Photographs of the NACA airfoil with the electrodes and Kapton film in place are shown in the photograph in Figure 3.10. The actuator spanned most of the width of the airfoil. A narrow gap was left at the location of the pressure taps, although both sides were electrically connected together.

3.3.2 Motor

The airfoil were capable of being oscillated or dynamically-pitched about its quarter chord location about any mean angle with any range of angles. The motion was driven by a specially selected servo motor (SmartMotor SM3430 by Animatics) shown in Figure 3.12. This had a 10:1 gear drive and provided 11 N·m (96.8 lb·in) of continuous torque. The controller program, which was stored in the motor internal circuitry, moved the motor in response to an input voltage. The SmartMotor Interface software

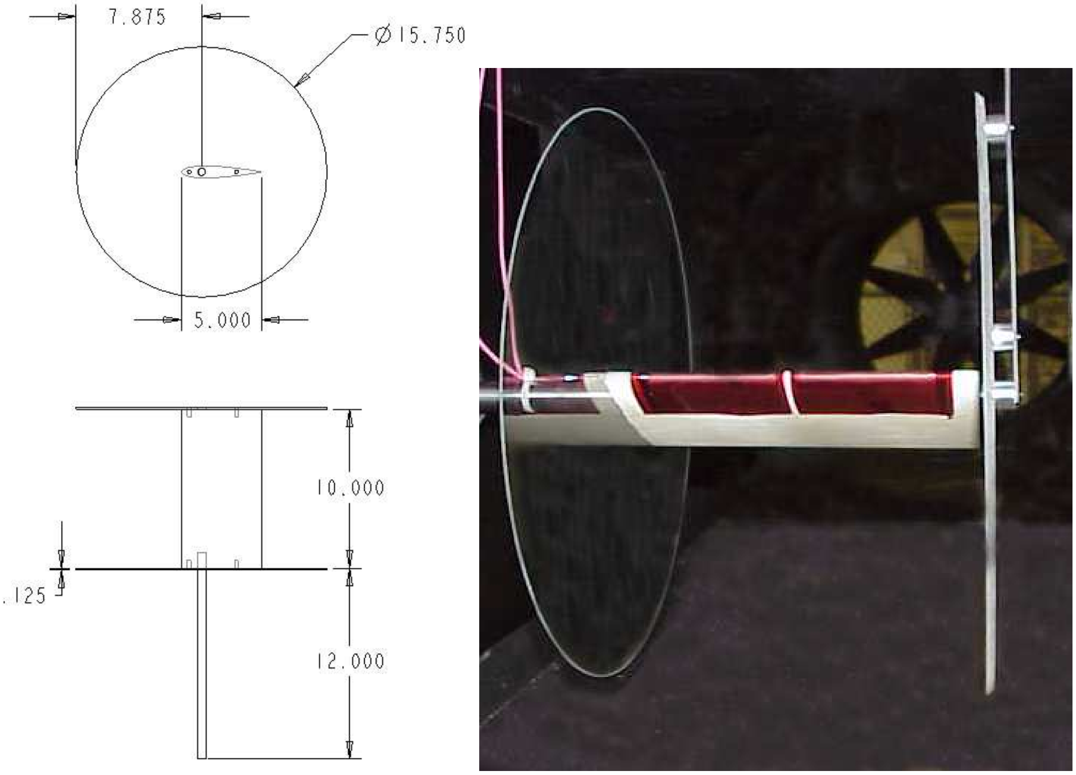

Figure 3.10. Schematic drawing and photograph of the NACA 0015 airfoil with circular end plates. Dimensions are in inches.

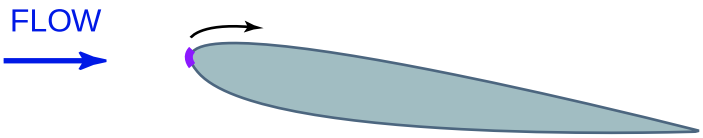

Figure 3.11. Schematic drawing showing the location and orientation of plasma actuator on the NACA 0015.

was used to modify the controller program, which is in Appendix A.

A Stanford Research Systems DS335 3.1 MHz synthesized function generator was used to oscillate the airfoil sinusoidally. The oscillatory airfoil motion was defined by

$$\alpha = \alpha_0 + \alpha_1 \sin \omega t \tag{3.6}$$

where α is the angle of attack, α_0 is the mean angle of attack, α_1 is the alternating angle of attack, ω is the frequency of oscillation, and t is the time.

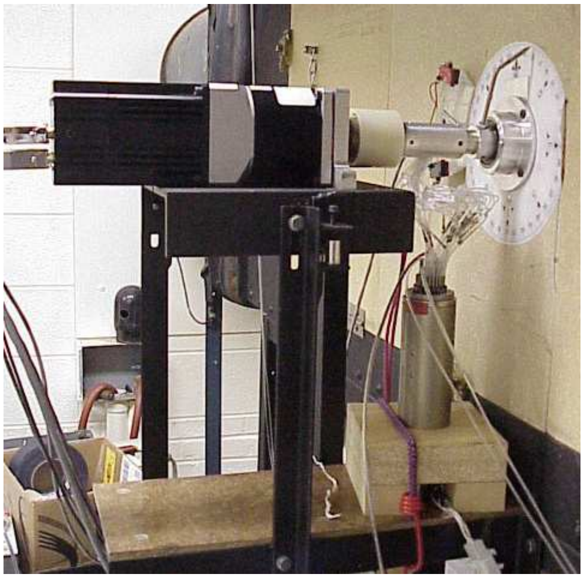

Figure 3.12. Photograph of the motor on the back wall of the test section.

Motor Position and Direction Circuit

Two 1000-count encoder signals were used to determine the instantaneous position and direction of the motor. A motor position and direction circuit was designed, constructed and utilized to use the digital encoder signals to construct an analog voltage yielding the motor position. A schematic of the circuit is shown in Figure 3.13, and a photograph of the actual circuit is shown in Figure 3.14.

The main components of the motor position and direction circuit and their operation are as follows:

P85A: The P85A is a 1 MHz crystal signal generator. It generates the clock pulses for the circuit.

4017 and 4013: The 4017 and 4013 chips divide down the clock by ten and two, respectively.

HP2020: The HP2020 chip is a quadrature decoder. It uses the two encoder output signals (A and B) as inputs, and generates a pulse and a direction on every rising and falling edge.

4049: The 4049 is a hex inverter, which is used to invert some of the digital signals as needed.

LS191: The four LS191 chips are 4-bit up/down binary counters that increment (or decrement) with each pulse of the HP2020.

4047: The 4047 is a 1-shot pulse generator that resets the counters to zero. The

MSB of the counter array is inverted so as to position the count at mid-range. The counters have been cascaded and are inputed to the LTC1597.

LTC1597: The LTC1597 is a 16-bit Digital-to-Analog (D/A) converter.

1112: The 1112 is a current to voltage op-amp. It converts the output of the D/A converter to a voltage that corresponds to the airfoil's position.

LT1236-10 The LT1236-10 regulates a precise 10 volts. It serves as the reference for the LTC1597.

A comparison of the function generator input to the motor and output from the motor position and direction circuit is shown in Figure 3.15. It shows recorded time series from a LeCroy LT342L oscilloscope. One period corresponds to 4 hz. The top trace is the function generator sine wave input to the motor. The bottom trace is the actual instantaneous position of the motor as determined from the motor encoder. Comparing the two traces, it is clear that the actual instantaneous motor position is sinusoidal, but lags in phase behind the function generator. For this reason the function generator input cannot be sampled to determine the motor's position. The output from the motor position and direction was sample as the instantaneous motor position.

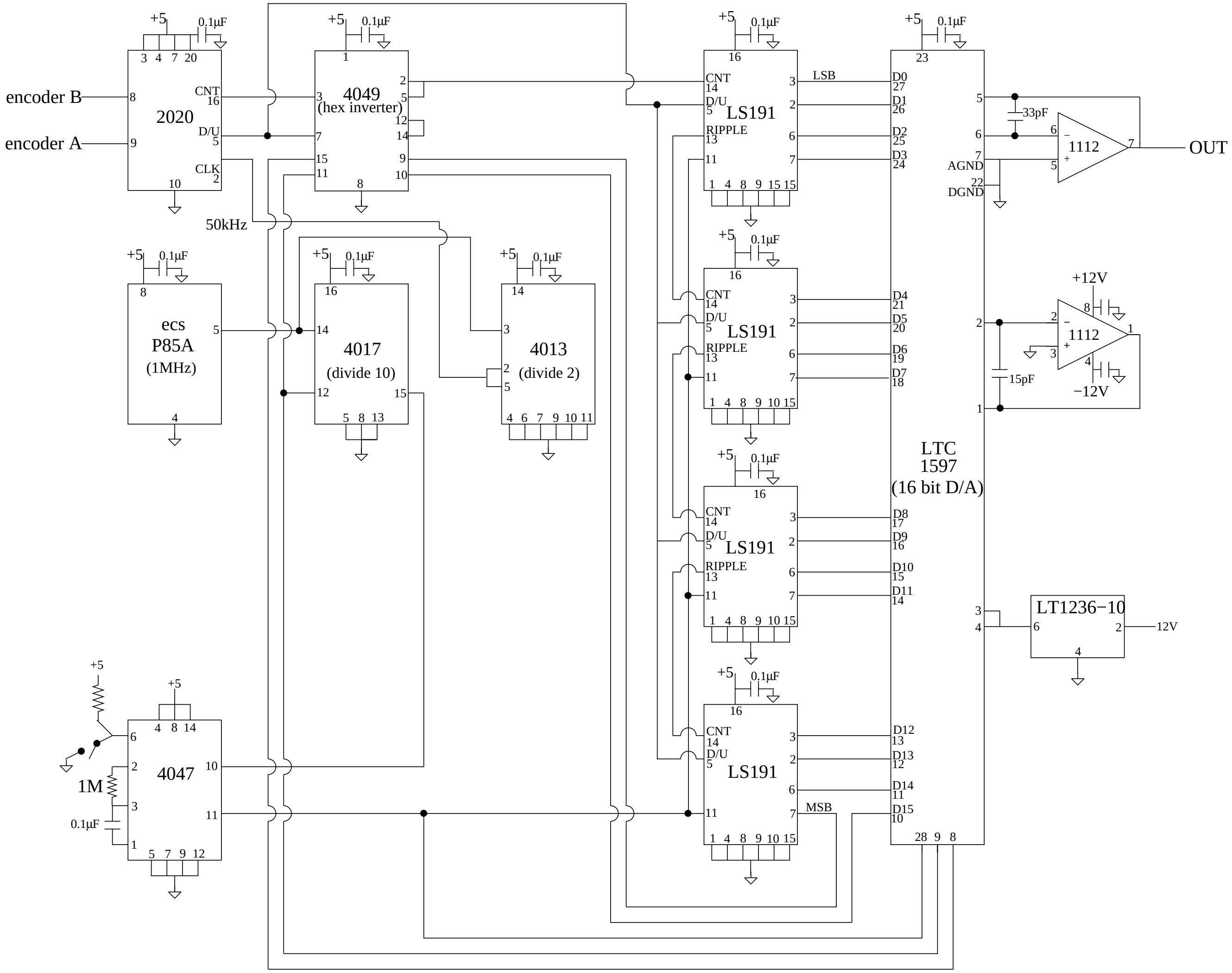

Figure 3.13. Schematic of the circuit that uses the motor encoder as an input to output the instantaneous airfoil position and direction.

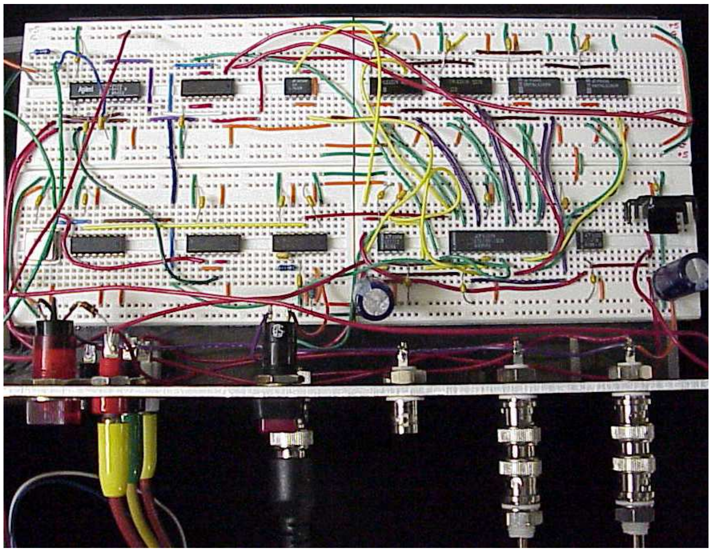

Figure 3.14. A photograph of the motor position and direction circuit.

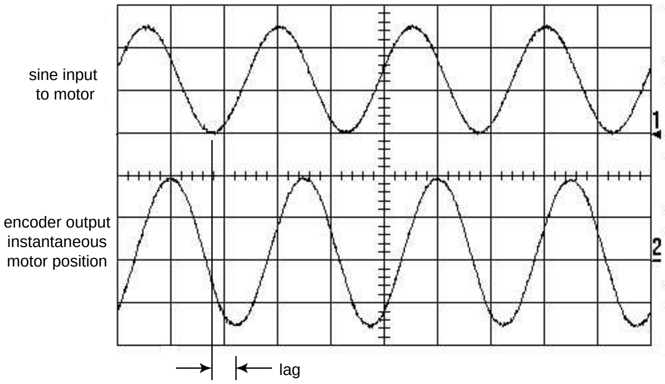

Figure 3.15. Oscilloscope trace of the sine input to the motor (top) and the actual position of the motor (bottom).

Angle of Attack Indicator Circuit

The instantaneous angle of attack of the airfoil needed to be known. For example, the strobe for flow visualization required a trigger input for any particular angle of attack. For "smart" actuator operation, the angle of attack was needed to serve as a reference of when to turn off and on the plasma actuator. For these reasons, an angle of attack indicator circuit was designed and constructed to output a square wave pulse about each integer angle of attack. A schematic of the angle of attack indicator circuit is shown in Figure 3.16, and a photograph of the actual circuit is shown in Figure 3.17.

The output of the motor position and direction circuit was an analog signal that provided an indication of the motor position, which corresponded to different angles of attack. The voltage amplitude of the signal was calibrated to determine the voltages corresponding to integer angles of attack.

The angle of attack indicator circuit consisted of two components: (1) conditioned the motor position and direction signal and set the window-width voltage and (2) generated the square wave pulse at each voltage that corresponded to an integer angle of attack. The top circuit diagram in Figure 3.16 conditioned the input signal and set the window-width voltage. The input signal was gained using a variable resistor to increase signal resolution, and offset by another variable resistor to allow for single-sided operation. The signals were buffered by a LM324.

The bottom circuit diagram in Figure 3.16 generated the square wave pulse at each voltage that corresponded to an integer angle of attack. Two circuits are shown;

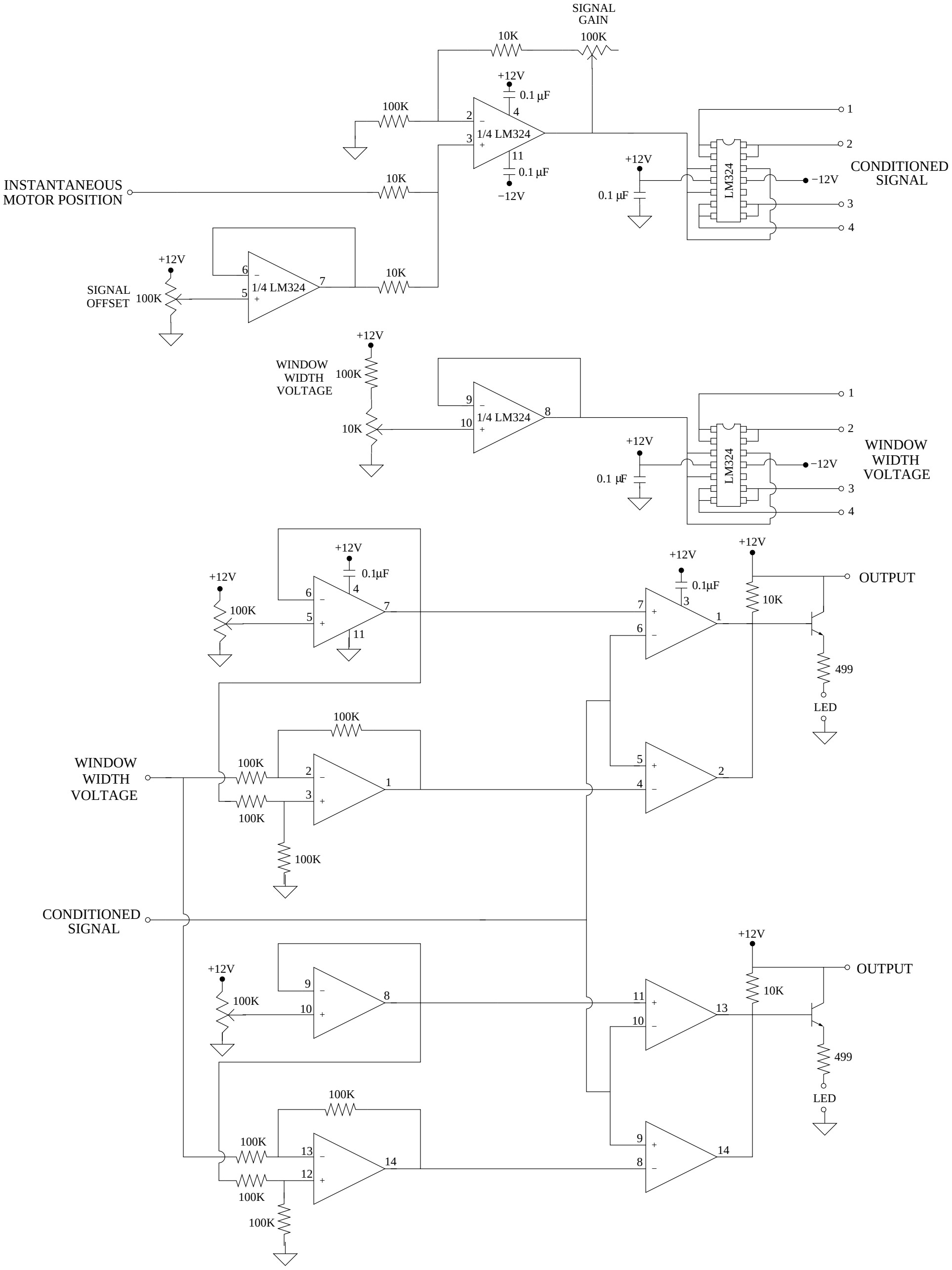

Figure 3.16. Schematic of the two circuits that comprise the angle of attack indicator circuit.

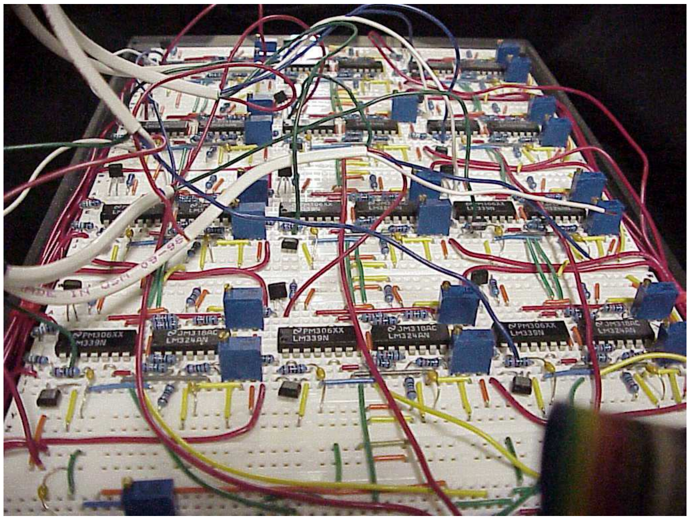

Figure 3.17. A photograph of the angle of attack indicator circuit.

however, a total of 21 circuits were constructed and used to accommodate 21 different angles of attack. The input for the bottom circuit in Figure 3.16 are the conditioned signal and window-width voltage from the top circuit in Figure 3.16. A variable resistor was used to set a high-voltage limit, based on the calibration, for each integer angle of attack. To obtain the low-voltage limit, a difference amplifier subtracted the window-width voltage from the high-voltage limit. A window comparator generated a square wave pulse between the low-voltage limit and high-voltage limit for each integer angle of attack. This pulse was also used to light a rainbow array of LEDs to serve as a visual reference for the angle of attack

“Smart” Actuation Circuit

A single signal was needed to turn off and on the 5 kHz driving frequency for the plasma to the “smart” operation. Therefore the “smart” actuation circuit was designed and constructed. A schematic of the “smart” actuation circuit is shown in Figure 3.18, and a photograph of the actual circuit is shown in Figure 3.19.

There were three inputs to the “smart” actuation circuit: (1) the 5 kHz driving frequency for the plasma, (2) the up/down direction signal indicator from the motor position and direction circuit, and (3) the square wave pulse(s) from the angle of attack indicator circuit to determine between which angles of attack plasma actuation was desired.

The main components of the “smart” actuation circuit and their operation are as follows:

4050: The 4050 is a hex non-inverting buffer and TTL driver. Signals from the angle of attack indicator circuit were buffered and conditioned to a 5 V TTL.

74LS08: The 74LS08 is a quad, two-input ‘and’ gate. The up/down direction signal from the motor position and direction circuit was used along with the angle of attack signals from the angle of attack indicator circuit in an ‘and’ gate.

74LS112: The 74LS112 is a flop-flop used to generate a signal high between the ‘ON’ and ‘OFF’ voltage range. When a high signal was received on the ‘ON’ input, the output of the flip-flop was set high. When a high signal was received on the ‘OFF’ input, the output of the flip-flop was set low. When neither input was

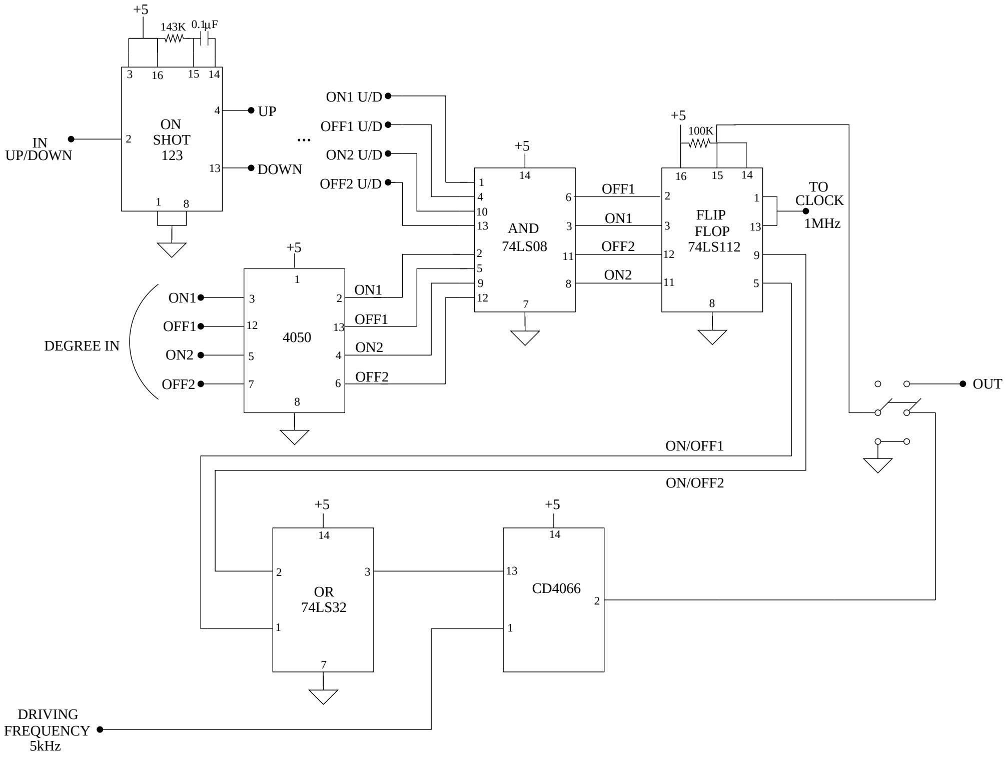

Figure 3.18. Schematic of the circuit that generates a signal for the "smart" actuation operation.

active, the output of the flip-flop would maintain its previous state.

74LS32: The 74LS32 is a quad, two-input 'or' gate. It was used to combine multiple on/off signals to a single signal.

CD4066: The CD4066 is a quad, bilateral switch that requires two inputs. The single output signal from the 74LS32 was used to drive the CD4066 to turn off and on the 5 kHz driving frequency for the plasma.

An oscilloscope trace of the 5 kHz used to generate the plasma and the "smart" actuation signal generated by the "smart" actuation circuit is shown in Figure 3.20.

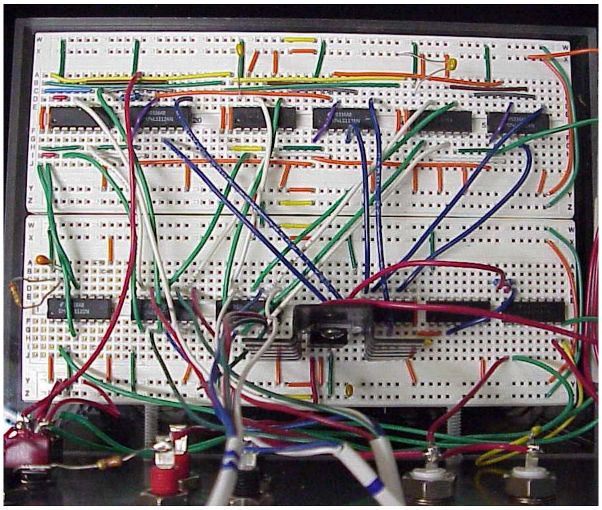

Figure 3.19. A photograph of the “smart” actuation circuit.

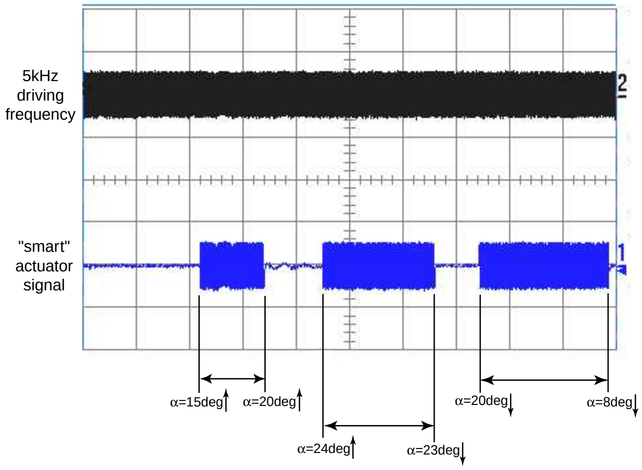

Figure 3.20. Oscilloscope trace of the 5 kHz used to generate the plasma (top) and the “smart” actuation trace (bottom).

3.3.3 Pressure Data Acquisition

A total of 29 surface pressure ports, 0.5 mm (0.02 in) I.D., were aligned with the flow direction at the half-span location on the airfoil. Although they were spaced relatively uniformly around the airfoil, there was a slight increase in concentration of ports near the leading edge. Table 3.2 provides the positions of the surface pressure ports.

Table 3.2. Static pressure port locations on the surface of the oscillating airfoil.

Port #	x/c	Port #	x/c
0	0.0		
1/2	0.025	15/16	0.0456
3/4	0.051	17/18	0.532
5/6	0.076	19/20	0.608
7/8	0.152	21/22	0.684
9/10	0.228	23/24	0.759
11/12	0.304	25/26	0.835
13/14	0.380	27/28	0.911

The pressure measurements were made utilizing a Scanivalve Model J9 scanning pressure valve. A Scanivalve PDCR24 differential pressure transducer having a range of ±10 in H_2O was used with the oscillating airfoil. This transducer was chosen because it mounted inside the Scanivalve cavity and had a good published frequency response.

The signal from the transducer was gained, filtered, and buffered. A transducer conditioning circuit was designed, built, and used during the data acquisition. A schematic of the transducer condition circuit is shown in Figure 3.21. The transducer is represented as the Wheatstone Bridge at the top of the circuit diagram. The signal gain of 500 was set by the ratio of the resistance in the Wheatstone Bridge, 4 kΩ, to the resistor in the amplifying circuit, $2\,\mathrm{M}\Omega$. This approximation assumes that the values of resistance in the bridge are much smaller than the resistors in the amplifying circuit. For this experiment,

$$\text{Gain} = \frac{R_{amplifier}}{R_{bridge}} = \frac{2\text{M}}{4\text{k}} = 500. \tag{3.7}$$

The signal was filtered using a second-order, Butterworth filter, shown in the middle circuit in Figure 3.21. The cut-off frequency, f_c, for the low-pass filter is related to the resistance and capacitance of the circuit and damping factor. This relationship is

$$f_c = \frac{1}{2\pi R C_1 \xi}, \tag{3.8}$$

where ξ is the damping factor, defined as for the transducer conditioning circuit in Figure 3.21 as

$$\xi = \left(\frac{C}{C_1}\right)^{1/2} = \frac{0.0047}{0.01} = 0.685. \tag{3.9}$$

Setting the cut-off frequency to 200 Hz and solving for the resistance in Equation 3.8 gives the value of the resistors for the filter circuit,

$$R = \frac{1}{2\pi f_c \xi C_1} = \frac{1}{2\pi(0.685)(200)(0.01\times10^{-6})} = 116K \approx 120K. \tag{3.10}$$

Finally, the transducer conditioning circuit buffered the signal using a simple voltage follower, depicted in the bottom circuit in Figure 3.21. Static calibration of the Scanivalve pressure transducer resulted in a calibration coefficient of 2.17 volts/in. H_2O, as shown in Figure 3.23.

Dynamic calibration was performed by introducing a constant amplitude, varying frequency sinusoidal pressure fluctuation through one port on the NACA 0015 airfoil.

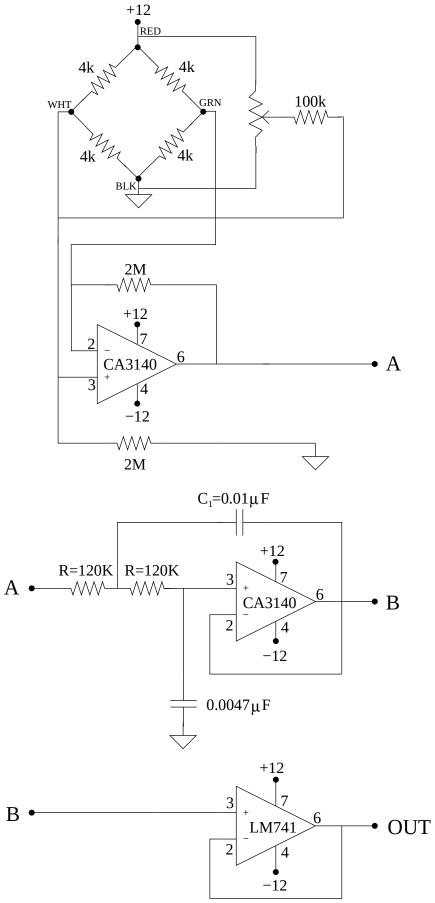

Figure 3.21. Schematic of the circuit used to condition the output signal from the Scanivalve pressure transducer.

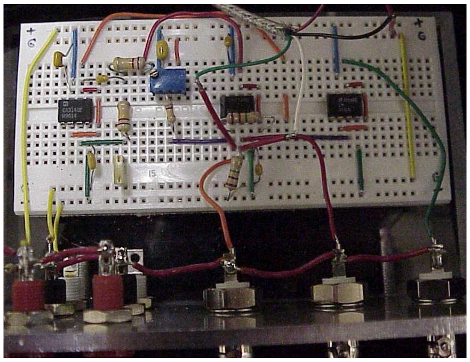

Figure 3.22. Photograph of the circuit used to condition the output signal from the Scanivalve pressure transducer.

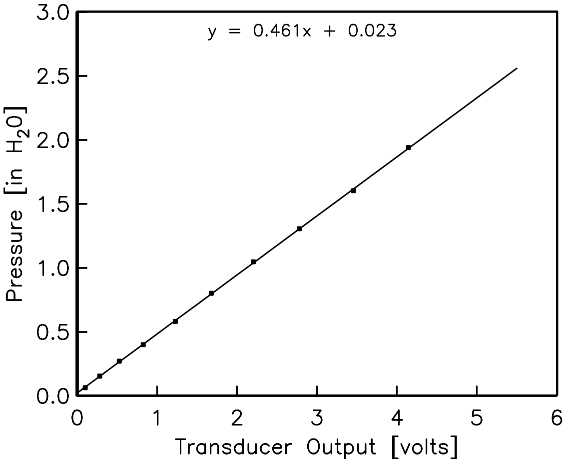

Figure 3.23. Static calibration curve for the Scanivalve PDCR24 pressure transducer.

The output of a Stanford Research Systems DS335 3.1 MHz Synthesized Function Generator boosted by a Crown D150A amplifier, drove a 0.127 m (5 in) speaker to provide the fluctuating pressure input. A 0.127 m (5 in) diameter, 0.1651 m (6.5 in) length can with a 0.003175 m (0.125 in) exit hole with an o-ring seal channeled the pressure fluctuations to the one pressure port on the model. An ACO microphone was used to monitor the fluctuations. The calibration consisted of recording the r.m.s. of the amplified transducer output and phase delay for various input frequencies. This was done by monitoring both the transducer and microphone signals on a LeCroy LT342L oscilloscope.

The total pressure measurement system had a 3 dB flat frequency response up to 150 Hz, as indicated in Figure 3.24. The phase response of the pressure system is shown in Figure 3.25. The maximum physical frequency of airfoil oscillation was 4 Hz. The frequencies which held most of the structures or energy ??? what to write here ??? were assumed to be less than 150 Hz. Therefore, no corrections were made to the data and with the pressure transducer.

For wind tunnel operations, a pitot static probe located in the freesteam provided the reference static pressure for each pressure port. A second pitot static probe was mounted to a traversing mechanism two chord lengths downstream of the airfoil in its spanwise centerline. Discrete points were sampled across the wake to construct the mean velocity profile.

On the surface of the airfoil, the coefficient of pressure, C_p, was calculated as

$$C_p = \frac{P_s - P_\infty}{\frac{1}{2}\rho U_\infty^2} = \frac{P_s - P_\infty}{P_0 - P_\infty} \tag{3.11}$$

where P_s is the static pressure at each port, P_∞ is the static pressure of the freestream, ρ is the density of the freestream air, U_∞ is the velocity of the freestream, and P_0 is the total pressure of the freestream.

The coefficient of lift, C_l, was found by integrating the C_p distribution around the airfoil. Since high angles of attack were investigated with the oscillating airfoil, the coefficient of lift was calculated using

$$C_l = C_n \cos\alpha - C_a \sin\alpha \tag{3.12}$$

where c_n is the normal force coefficient given by

$$C_n = \int_0^1 (C_p^L - C_p^U) d\left(\frac{x}{c}\right) \tag{3.13}$$

and c_a is the axial force coefficient given by

$$C_a = \int_0^1 \left(C_p^U\left(\frac{dy_U}{c}\right) - C_p^L\left(\frac{dy_L}{c}\right)\right) d\left(\frac{x}{c}\right), \tag{3.14}$$

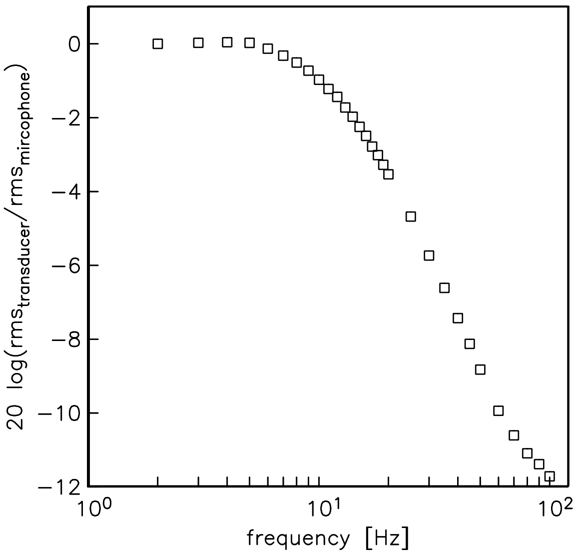

Figure 3.24. Dynamic calibration of the Scanivalve PDCR24 pressure transducer.

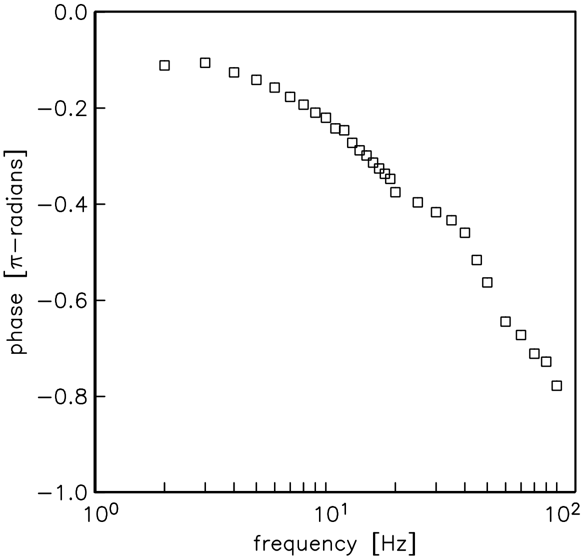

Figure 3.25. Phase lag of the Scanivalve PDCR24 pressure transducer.

where the subscripts and superscripts of U and L refer to the upper and lower surface of the airfoil, respectfully.

The moment coefficient, C_m, was calculated at the leading edge LE using

$$C_{m_{LE}} = -\frac{1}{c^2}\int_0^1 (C_p^L - C_p^U)\frac{x}{c} d\left(\frac{x}{c}\right). \tag{3.15}$$

The moment coefficient was transferred to the quarter-chord by

$$C_{m_{1/4}} = C_{m_{LE}} + \left(\frac{x}{c}\right) C_n. \tag{3.16}$$

Data acquisition was performed using a LabView program. For the oscillating airfoil, the pressure acquisition system worked as follows:

1. a pressure port was selected,
2. a time delay occurred to allow for the response of the Scanivalve,
3. pressure time series were acquired in a continuous record for a user-defined number of pitching cycles (typically 20 oscillations),
4. the time-series record was stored,
5. cycle-based ensemble averages and standard deviations were computed and stored for a number of discrete angles, and
6. another pressure port was selected and the acquisition steps were repeated until all of the pressure ports had been sampled.

Post data processing was done using Matlab. A program was written to calculate the coefficients of lift and moment using the previously given definitions. It can be found in Appendix B.

APPENDIX A

SMARTMOTOR PROGRAM

This program was used by the motor through the Smartmotor Interface Software to oscillate the airfoil. For different physical oscillation frequencies, the motor's velocity and acceleration needed to be changed through this program. The range of angles of attack was also controlled by this program by scaling the analog input accordingly. The motor encoder was quadrature and the motor head a 10:1 gear drive, so there were $4,000 \times 10 = 40,000$ encoder counts per cycle. Each cycle was 360 degrees, which resulted in 111.1111111111 encouder counts per physical degree. The analog input from the function generator had an amplitude of 5V and was scaled by the program to 1023.

```
'Notre Dame Wing Flapper Program
'Scale factor:  1 deg = 111.1111111111 counts
'Calculate the distance and round off to the nearest integer.
'Set up Limit inputs/Home Complete output
    LIMD  'Directional Limits
    LIMH  'Set limit active high
'Set up tuning values
```

```
    KP=250   'Proportional gain
    KI=350   'Integral gain
    KD=2200  'Differential gain
    KL=100   'Integral limit
    KS=1     'Sample speed
    KV=500   'Velocity feed-forward
    KA=250   'Acceleration feed-forward
    KG=0     'Gravity gain
    F        'Set values
    F=8      'Improve settling time
    E=1000   'Following error limit
    RUN?     'Wait for run command
    O=0      'Set origin to current position
'Read analog input (0-5VDC = -10-10 deg on gearhead shaft)
'Allow motion to match analog input
    UGI             'Set up pin G as analog input
    'A=4500         'Acceleration necessary for 5Hz
    'V=580000       'Velocity necessary for 5Hz
    A=2880          'for 4Hz
    V=464000        'for 4Hz
    'A=2205         'for 3.5Hz
    'V=406000       'for 3.5Hz
    'A=1630         'for 3Hz
    'V=348000       'for 3Hz
    'A=1125         'for 2.5Hz
    'V=290000       'for 2.5Hz
    'A=720          'for 1-2Hz
    'V=232000       'for 1-2Hz
    'A=6480
    'V=696000
    WHILE 1         'Infinite loop
    g=UGA           'Read analog input
                    'For 20 deg (+/-10) degree range
    g=g*800000      'Start scaling of analog input
    g=409200000-g   'Finish scaling of analog input
    'g=g*400000     'For 10 deg (+/-5) degree range
    'g=204600000-g  'For 10 deg (+/-5) degree range
    'g=g*640000     'For 16 deg (+/-8) degree range
    'g=327360000-g  'For 16 deg (+/-8) degree range
    g=g/368280
    P=g             'Set new position
    G               'Start motion
    LOOP
    END
```

APPENDIX B

ERROR ANALYSIS

Experimental uncertainty analysis involves the identification of errors that arise during all stages of the experiment and the propagation of these errors into the overall uncertainty of a desired result. It is the result of both systematic (bias) and random (precision) errors. The systematic error is a resolution error associated with a particular measurement. The random error considers the repeatability of data, independent of the measurement tools. Systematic error is relatively easy to quanitify, while random error depends on statistics to quantify.

Most experiments can be caregorized either as timewise or sample-to-sample [17]. The work here was exclusively sample-to-sample experimentation. In a sample-to-sample experiment, the random error comes from both measurement system variability and variations due to small, uncontrollable factors during the measurement.

An A/D converter translates analog signal information into a digital format used by a computer. A 12-bit A/D converter was used in this work, which means that the signal's amplitude was represented by a finite set of 2^{12} values. This can be a source of error known as the absolute quantization error of the A/D converter. The resolution, Q, of a 12-bit converter with a full scale range of -10 V to 10 V is given by

$$Q = \frac{E_{FSR}}{2^{12}} = \frac{20}{4096} = 0.00488\,\mathrm{V/bit} \tag{B.1}$$

where E_{FSR} is the full scale range of the voltage. The quantization error per bit, e_Q, is

$$e_Q = \frac{1}{2}Q = 0.00244\,\mathrm{V/bit}. \tag{B.2}$$

Random uncertainty can be characterized by the standard deviation of the random error. The random uncertainty, P_V, in the average voltage, $\bar{V}$, is given by

$$P_{\bar{V}} = t_{\nu_{P_V},C} \cdot S_{P_V}, \tag{B.3}$$

where $t_{\nu_{P_V},C}$ is the Student's t variable, ν_{P_V} is the number of degrees of freedom, and C is the confidence level. The number of degrees of freedom is

$$\nu = N - c, \tag{B.4}$$

where N is the number of samples and c is the number of independent constraints. The standard confidence assumtion is 95%.

For the oscillating airfoil, the standard deviation of the pressure measurement was calculated. When computing the standard deviation, the value of the mean is required, so there is one constaint and $c = 1$. With $N = 20$ and $c = 1$ using table from Dunn [17], the corresponding $t_{\nu,P}$ is ±2.093. This means that there is a 95% probability that a sample value will be within ±2.093 sample standard deviations of the sample mean. The random uncertainty for the voltage measurement for the oscillating airfoil is

$$P_{\bar{V}} = \pm 2.093(0.02) = 0.042\,\mathrm{V} \tag{B.5}$$

The lift and drag data are results that depend upon the integral of measured values at discrete locations. This may result in a discretization error.

BIBLIOGRAPHY

[1] Abbott, I.H. and A.E. Von Doenhoff. 1959. "Theory of Wing Sections." Dover Publications, Inc.; New York.

[2] Anderson Jr., J.D. 1989. "Introduction to Flight." McGraw-Hill, Inc.; New York.

[3] Anderson Jr., J.D. 2001. "Fundamentals of Aerodynamics." McGraw-Hill, Inc.; New York.

[4] Birch, D. and T. Lee. "Measurement of the Boundary Layer Developed on an Oscillating Airfoil." Department of Mechanical Engineering, McGill University, Montreal, Quebec, Canada.

[5] Bragg, M.B. and G.M. Gregorek. 1987. "Experimental Study of Airfoil Performance with Vortex Generators." *J. Aircraft*, Volume 24, Number 5, pg 305-309.

[6] Briley, W.R. and H. McDonald. 1975. "Numerical prediction of incompressible separation bubbles." *Journal of Fluid Mechanics*, Volume 69, Part 4, pg 631-656.

[7] Brown, S. 1966. "Introduction to Electrical Discharges in Gases." John Wiley and Sons, Inc.: New York.

[8] Cavalieri, D. 1995. "On the Experimental Design for Instability Analysis on a Cone at Mach 3.5 and 6 Using a Corona Discharge Perturbation Method." M.S. Thesis, Illinois Institute of Technology.

[9] Chang, P.K. 1976. "Control of Flow Separation." Hemisphere Publishing Corporation; Washington.

[10] Corke, T.C. 2002. "Design of Aircraft." Prentive-Hall Publishers; New York.

[11] Corke, T.C. and D. Cavalieri. 1997. "Controlled Experiments on Instabilities and Transition to Turbulence in Supersonic Boundary Layers." *AIAA 97-1817*.

[12] Corke, T., D. Cavalieri, and E. Matlis. 2001. "Boundary layer instability on a sharp cone at Mach 3.5 with controlled input." *AIAA Journal*, 40, 5, pg. 1015.

[13] Corke, T., E. Jumper, M. Post, D. Orlov, and T. McLaughlin. 2002. "Application of weakly-ionized plasmas as wing flow-control devices." *AIAA Paper 2002-0350*, AIAA Journal, in review.

[14] Corke, T. C. and E. Matlis. 2000. "Phased Plasma Arrays for Unsteady Flow Control." *AIAA 2000-2323*.

[15] Curle, N. 1962. “The Laminar Boundary Layer Equations.” Clarendon Press: Oxford.

[16] Curle, N. and S.W. Skan. 1957. “Approximate Methods for Predicting Separation Properties of Laminar Boundary Layers.” *Aeronautical Quarterly*, Volume 8, pg 113-144.

[17] Dunn, P.F. 2005. “Measurement and Data Analysis for Engineering and Science.” McGraw-Hill.

[18] Enloe, L., T. McLaughlin, VanDyken, Kachner, E. Jumper, and T. Corke. 2003. “Mechanisms and Response of a single dielectric barrier plasma.” *AIAA 2003-1021.*

[19] Enloe, L., T. McLaughlin, and R. VanDyken. 2004. “Plasma Structure in the Aerodynamic Plasma Actuator.” *AIAA 2004-0844*.

[20] Eppler, R. 1999. “Airfoils with boundary layer suction, design and off-design cases.” *Aerospace Science Technology*, Volume 3, pg. 403-415.

[21] Erturk, Ercan. 2000. Internal collaboration at the University of Notre Dame.

[22] Erturk, E. and T. C. Corke. 2000. “Formulation for Highly Accurate Solutions of the 2-D Navier-Stokes Equations at high Reynolds numbers.” In review *Journal Comp. Physics.*

[23] Erturk, E. and T.C. Corke. 2001. “Boundary Layer Leading Edge Receptivity to Sound at Incidence Angles.” Accepted for publication *Journal of Fluid Mechanics.*

[24] Fink, D. and D. Christiansen. 1982. “Electronics Engineers’ Handbook.” McGraw-Hill Book Company: New York.

[25] Gad-el-Hak, M. 2000. “Flow Control: Passive, Active, and Reactive Flow Management.” Cambridge University Press; New York.

[26] Gad-el-Hak, M. and D. Bushnell. 1991. “Separation Control: Review.” *Journal of Fluids Engineering*, Volume 115, pg 5-30.

[27] Gadri, R. and J. R. Roth. 1998. “Glow discharge-like characteristics of a OAUGDP revealed by computer modeling.” 25th IEEE International Conference on Plasma Science.

[28] Glanz, James. “The Pervasive Plasma State.” An essay from a brochure prepared by the Division of Plasma Physics of the American Physical Society.

[29] Glauert, M.B. 1956. “The Wall Jet.” *Journal of Fluid Mechanics*, Volume 1, pg 625.

[30] Glezer, A., M.G. Allen, D.J. Coe, S.L. Barton, M.A. Trautman, and J.W. Wiltse. 1998. “Synthetic Jet Actuator and Applications Thereof.” U.S. Patent 5,758,823.

[31] Goldstein, R.J. (Editor) and T. Mueller (Chapter 6: Flow Visualization by Direct Injection). 1996. "Fluid Mechanics Measurements." Taylor and Francis: Washington D.C.

[32] Greenblatt, D. and I. Wygnanski. 2000. "The control of separation by period excitation." *Progress in Aerospace Sciences*, Volume 36, pg 487-545.

[33] Graeme, J., G. Tobey, and L. Huelsman. 1971. "Operational Amplifiers: Design and Applications." Burr-Brown. McGraw-Hill Book Company, New York.

[34] Huang, J., T. Corke, and F. Thomas. 2003. "Plasma actuators for separation control of low pressure turbine blades." *AIAA Paper 2003-1027.*

[35] Hultgren, L.S. and D.E. Ashpis. 2003. "Demonstration of Separation Delay with Glow-Discharge Plasma Actuators." *AIAA 2003-1025.*

[36] Jansen, 1982. "Experimental studies of the effect of the laminar separation bubble on the performance of a NACA $66_3 - 018$ airfoil at low Reynolds numbers." M.S. Thesis, University of Notre Dame.

[37] Johnston, H. and J. Liu. 2002. "Finite Difference Schemes for Incompressible Flow Based on Local Pressure Boundary Conditions." *Journal of Computational Physics*, Volume 180, pg 120-154.

[38] Kanda, N., M. Kogoma, H. Jinno, H. Uchiyama, and S. Okazaki. 1991. In the Proceedings of the 10th Symposium on Plasma Chemistry, Volume 3, *Paper 3.2-20.*

[39] Kakuta, S., T. Kamata, and T. Makabe. 1995. "Study of surface charges on dielectric electrodes in a radio-frequency." *Journal of Applied Physics*, Volume 77, Number 3, pp 985-991.

[40] Kerho, M, S. Hutcherson, R.F. Blackwelder, and R.H. Liebeck. 1993. "Vortex generators used to control laminar separation bubbles." *Journal of Aircraft*, Volume 30, Number 3, pg 315-319.

[41] Khorrami, M.R., M. Choudhari, B.A. Singer, D.P. Lockard, and C.L. Streett. 2003. "In search of the physics: The interplay of experiment and computation in slat aeroacoustics." *AIAA 2003-0980.*

[42] Lachowicz, J., C. Yao, and R. Wlezien. 1998. "Scaling of an Oscillatory Flow Control Actuator." *AIAA 98-0330.*

[43] Lachmann, G.V. (Editor) 1961. "Boundary Layer and Flow Control: Volume I and Volume II." Pergamon Press; New York.

[44] Lee, C. and D. Goldstein. 2000. "Two-Dimensional Synthetic Jet Simulation." *AIAA 2000-0406.*

[45] Leishman, J. Gordon. 2000. "Principles of Helicopter Aerodynamics." Cambridge University Press, New York

[46] Lin, J.C., S.K. Robinson, and R.J. McGhee. 1994. "Separation control on high-lift airfoils via micro-vortex generators." *Journal of Aircraft*, Volume 31, Number 6, pg 1317-1323.

[47] Lin, J.C. 2002. "Review of research on low-profile vortex generators to control boundary-layer separation." it Progress in Aerospace Sciences, Volume 38, pg 389-420.

[48] Lorder P., D. McCormick, T. Anderson, B. Wake, and D. MacMartin. 2000. "Rotorcraft Retreating Blade Stall Control." *AIAA 2000-2475.*

[49] Malik, M., L. Weinstein, and M. Hussaini. 1983. "Ion Wind Drag Reduction." In the Proceedings of the AIAA 21st Aerospace Sciences Meeting.

[50] Massines, F., A. Rabehi, P. Decomps, R Gadri, P. Segur, & C. Mayoux. 1998. "Experimental and Theoretical Study of a Glow Discharge at Atmospheric Pressure Controlled by a Dielectric Barrier." *Journal of Applied Physics*, Volume 83, Number 6, pp. 2950-2957.

[51] McCormick, D. 2000. "Boundary Layer Separation Control with Directed Synthetic Jets." *AIAA 2000-0519.*

[52] McCormick, D., S. Lozyniak, D. MacMartin, and P. Lorder. 2001. "Compact, High-Power Boundary Layer Separation Control Actuation Development." In the Proceedings of the 2001 ASME Fluids Engineering Division Summer Meeting, New Orleans, Louisiana.

[53] McDaniel, Earl W. 1964. "Collision Phenomena in Ionized Gases." John Wiley and Sons, Inc.: New York.

[54] McLaughlin, T., L. Enloe. and R. VanDyken. 2003. "Mechanisms and response of a single dielectric barrier plasma." *AIAA Paper 2003-1021.*

[55] Meek, L. and Craigs, J. 1978. "Electrical Breakdown of Gases." John Wiley and Sons, Inc: New York.

[56] Mendoza, J.M., T.F. Brooks, and W.H. Humphreys, Jr. 2002. "Aeroacoustic Measurements of a Wing/Slat Model." *AIAA 2002-2604.*

[57] Mueller, T. J. 1980. "On the historical development of apparatus and techniques for smoke visualization of subsonic and supersonic flows." *AIAA Paper 80-0420-CP.*

[58] Nagib, H., J. Kiedaisch, D. Greenblatt, I. Wygnanski, and A. Hassen. 2001. "Effective flow control for rotorcraft applications at flight Mach numbers." *AIAA 2001-2974.*

[59] Olson, S. 2003. "Slat Tonal Noise Mechanisms in a Two-Dimensional Multi-Element Airfoil Configuration." PhD Thesis, University of Notre Dame.

[60] Orlov, D., E. Erturk, M. Post, and T. and Corke. 2001. "DNS Modeling of Plasma Array Flow Actuators." Bulletin of the American Physical Society Fluid Dynamics Division, Annual Meeting.

[61] Orlov, D., T. Corke, and M. Post, 2002. "DNS Modeling of plasma array flow actuators." Bulletin of the American Physical Society Fluid Dynamics Division, Annual Meeting.

[62] Orlov, D., T. Corke, and O. Haddad, 2003. "DNS Modeling of plasma actuators." Bulletin of the American Physical Society Fluid Dynamics Division, Annual Meeting.

[63] Patel, M.P. 2003. Orbital Research, Inc., conversation.

[64] Pai, S. T. 1992 "Analytic approach to glow discharge theory: The physical model." *Journal of Applied Physics*, Volume 71, Number 12, pp. 5820-5825.

[65] Post, M. L. 2001. "Phased plasma actuators for unsteady flow control." M.S. Thesis, University of Notre Dame.

[66] Post, M. and Corke, T. 2002. "Separation control using plasma actuators." Bulletin of the American Physical Society Fluid Dynamics Division, Annual Meeting.

[67] Post, M. and Corke T. 2003. "Separation control on high angle of attack airfoil using plasma actuators." *AIAA Paper 2003-1024.*

[68] Post, M. and T. Corke. 2003. "Airfoil Leading-edge Separation Control using Plasma Actuators." Bulletin of the American Physical Society Fluid Dynamics Division, Annual Meeting.

[69] Post, M. and Corke T. 2004. "Separation control using Plasma Actuators - Stationary and Oscillating Airfoils." *AIAA Paper 2004-0841.*

[70] Roth, J R., M. Laroussi, and C. Liu. 1992. "Experimental Generation of a steady-state Glow Discharge at Atmospheric Pressure." In the Proceedings of the 19th IEEE International Conference on Plasma Science.

[71] Roth, J.R. 1995. "Industrial Plasma Engineering." Institute of Physics Publishing.

[72] Roth, J.R., D. Sherman, and S. Wilkinson. 1998. "Boundary Layer Flow Control with One Atmosphere Uniform Glow Discharge Surface Plasma." *AIAA 1998-0238.*

[73] Roth, J.R., R. Madhan, M. Yadav, J. Rahel, and S. Wilkinson. 2004. "Flow Field Measurements of Paraelectric, Peristaltic, and Combined Plasma Actuators based on the One Atmosphere Uniform Glow Discharge Plasma (OAUGDP)." *AIAA 2004-0845.*

[74] Schlichting, H. 1960. "Boundary Layer Theory." McGraw-Hill Book Company, Inc.; New York.

[75] Schlichting, H. and W. Pachau. 1959. "Exakte Losungen fur dir laminar Grenzschicht mit Absaugung und Ausblasen." Dtsch. Akad. Luftfahrtforsch, 7B, pg 113. [9].

[76] Seifert, A., T. Bachar, D. Moss, M. Shepshelovish, and I. Wygnanski. 1993. "Oscillatory Blowing: A Tool to Delay Boundary-Layer Separation." *AIAA Journal*, Volume 11, Number 31, pg 2052-2060.

[77] Seifert, A., A. Darabi, and I. Wygnanski. 1996. "Delay of Airfoil Stall by Periodic Excitation." *Journal of Aircraft*, Volume 33, Number 4, pg 691-698.

[78] Seifert, A., S. Eliahu, and D. Greenblatt. 1998. "Use of piezoelectric actuators for airfoil separation control." *AIAA Journal*, Volume 36, Number 8, pg 1535-1537.

[79] Seifert, A., and L. Pack. "Oscillatory Excitation of Unsteady Compressible Flows over Airfoils at Flight Reynolds Numbers." *AIAA 99-0925*.

[80] Schubauer, G.B. and W.G. Spangenberg. 1960. "Forced mixing in boundary layers." *Journal of Fluid Mechanics*, Volume 8, pg 10-32.

[81] Smith, B.L. and A. Glezer. 1998. "The formation and evolution of synthetic jets." *Physics of Fluids*, Volume 10, Number 9, pg 2281-2297.

[82] Spitzer, Lyman, Jr. 1962. "Physics of Fully Ionized Gases." Interscience Publishers: New York.

[83] Stratford, B.S. 1959. "The prediction of separation of the turbulent boundary layer." *Journal of Fluid Mechanics*, Volume 5, pg 1-16.

[84] Sucec, J. 1995. "The double integral method applied to separation calculation." *International Journal of Heat Mass Transfer*, Volume 38, Number 15, pg 2771-2777.

[85] Taylor, H.D. 1947. "The elimination of diffuser separation by vortex generators." United Aircraft Corporation Report No. R-4012-3. [32].

[86] Thomas, Edward, Jr. 1999. "Direct measurements of two-dimensional velocity profiles in direct current glow discharge dusty plasmas." *Physics of Plasmas*, Volume 6, Number 7, pp. 2672-2675.

[87] Viswanath, P.R., G. Ramesh, and K.T. Madhavan. 2000. "Separation control by tangential blowing inside the bubble." *Experiments in Fluids*, Volume 29, pg 96-102.

[88] Volino, R.J. and L.S. Hultgren. 2000. "Measurements in separated and transitional boundary layers under low-pressure turbine turbine airfoil conditions." Proceedings of ASME Turbo Expo 2000.

[89] Volkov, V.N., 1965. "A Refinement of the Karman-Pohlhauser Integral Method in Boundary Layer Theory." *Journal of Engineering Physics*, Volume 9, Number 5, pg 371-374.

[90] Wilkinson, Steven. 2003. "Investigation of an Oscillating Surface Plasma for Turbulent Drag Reduction." *AIAA 2003-1023*.

[91] White, F.M. 1991. "Viscous Fluid Flow." McGraw-Hill, Inc.; New York.

[92] Yang, W. (Editor) and T. Mueller (Chapter 5: Gases-Smoke). 1989. "Handbook of Flow Visualization." Hemisphere Publishing Corporation: New York.

[93] Young, T.M., B. Humphreys, and J.P. Fielding. 2001. "Investigation of hybrid laminar flow control (HLFC) surfaces." *Aircraft Design*, Volume 4, pg 127-146.